Hypocenter Locations and Focal Mechanism Solutions of Earthquakes in the Epicentral Area of the 1886 Charleston, South Carolina, Earthquake

Anna Corella Hardy

Thesis submitted to the faculty of the Virginia Polytechnic Institute and State University in partial fulfillment of the requirements for the degree of

Master of Science
In
Geosciences

Committee Chair: Martin Chapman
John Hole
Ying Zhou

December 5th, 2014
Blacksburg, Virginia

Keywords: earthquakes, seismicity, seismic hazard, South Carolina

Hypocenter Locations and Focal Mechanism Solutions of Earthquakes in the Epicentral Area of the 1886 Charleston, South Carolina, Earthquake

Anna Corella Hardy

ABSTRACT

The Charleston earthquake of 1886 was one of the largest shocks to occur on the eastern coast of North America. The geological cause has long been a controversial issue and a variety of source models have been proposed. Previous potential field modeling and reinterpretation of seismic reflection and well data collected in the early 1980s indicate that the crust between approximately 1 and 4.5 km depth is comprised primarily of Mesozoic mafic rocks, with extensive faulting that is spatially coincident with modern seismicity in the epicentral area (Chapman and Beale, 2010).

This thesis proposes a new and testable hypothesis concerning the fault source of the 1886 shock that is very different from all previous interpretations. It is based on data collected during 2011-2012 from a local seismic network deployment in the immediate epicentral area. The 8-station temporary network was designed to better constrain earthquake hypocenter locations and focal mechanisms. Hypocenter locations of 134 earthquakes indicate a south-striking, west-dipping seismogenic zone in the upper 12 km of the crust. Over 40% of the 66 well-constrained focal mechanisms show reverse faulting on approximately north-south trending nodal planes, consistent with the orientation of the tabular hypocenter distribution.

I offer the following hypothesis: The 1886 shock occurred by compressional reactivation of a major, south-striking, west-dipping early Mesozoic extensional fault. The modern seismicity can be regarded as a long-term aftershock sequence that is outlining the 1886 damage zone. Variability of shallow focal mechanisms is due to the complex early Mesozoic fault structure in the upper 4-5 km.

Acknowledgements

I would first like to acknowledge the funding sources that made this research possible: award number G11AP20141 from the U.S. Geological Survey External Research Program, for the purpose of deploying the seismic network from which my dataset was derived.

I would like to acknowledge many people who have supported me throughout the past couple years. First and foremost, I would like to thank my advisor, Dr. Martin Chapman. He has always made himself available to help, teach, encourage, challenge, and support me, despite his extraordinarily busy schedule. I was fortunate to know him as a professor and research mentor as an undergraduate student, and I have continued to learn much from him as a graduate student. Finally, I want to thank him for his patience and kindness during many difficult challenges I faced in my graduate career, which at times affected my motivation and progress. I would like to extend this gratitude for patience and kindness to my committee members, Dr. John Hole and Dr. Ying Zhou. I also had the pleasure of having them as undergraduate professors, and I am grateful for all they have taught me, both in and out of the classroom. I would like to additionally thank Jake Beale, a research associate at the Virginia Tech Seismological Observatory (VTSO), who has been a great mentor and friend to me during this project.

I would also like to acknowledge the Department of Geosciences as a whole. The staff, including the main office administrators, technical support, museum coordinator Llyn Sharp, and especially Connie Lowe, has been a consistent source of support and assistance. In addition to the staff, I am also grateful for all the professors I have had the opportunity to work with and learn from.

I would also like to acknowledge the numerous students, both inside and outside the Department of Geosciences. The students involved in research at the VTSO have been an extremely valuable resource to me throughout the entire project, and I am extremely appreciative of their constant willingness to provide help and research resources to me. The other students in geophysics and in the department have been immensely supportive, and I am thankful for each and every one of them I have gotten to know. I would also like to thank the students and professors at the University of South Carolina for their collaborative research ideas and knowledge of the study region.

Finally, I would like to acknowledge my friends and family, without whom I would not be the person I am today. Their support, love, and encouragement have lifted me during challenging times and have made my life so rewarding every day.

Table of Contents

ABSTRACT....ii
Acknowledgements....iii
Table of Contents....iv
List of Figures....v
List of Tables....vi
List of Abbreviations....vii
Chapter 1: Introduction....1
1.1: The 1886 Charleston, South Carolina Earthquake....1
1.2: Overview of studies related to the 1886 Earthquake....2
1.3: Tectonic setting....3
1.4: Modern seismicity in South Carolina....5
1.5: Implications of seismicity....6
1.6: Project overview....7
Chapter 2. Data Processing and Methods....8
2.1: Data set and station network overview....8
2.2: Processing steps....8
2.3: Picking phase arrival times, polarities, and amplitudes....11
Chapter 3. Determining hypocenters....13
3.1: Locating hypocenters using Hypoellipse....13
3.2: Re-locating hypocenters using HypoDD....15
3.3: Plotting and analysis of hypocenters....18
3.4: Discussion and implications of results....20
Chapter 4. Determining focal mechanisms....22
4.1: Source characterization using focal mechanisms....22
4.2: Determining focal mechanisms using Focmec....24
4.3: Constraint testing....25
4.4: Plotting and analysis of focal mechanisms....26
4.5: Discussion and implications of results....27
Chapter 5. Conclusions....28
References....32
Appendix A: Figures....39
Chapter 1:....39
Chapter 2:....45
Chapter 3:....51
Chapter 4:....58
Appendix B: Tables....67

List of Figures

Chapter 1:
1.1: *A diagram showing the Modified Mercalli Intensity (MMI) Scale*.....39
1.2: *A contoured MMI map for the 1886 Charleston, earthquake*.....40
1.3: *A proposed fault model for the study region*.....41
1.4: *Detailed maps of the study region*.....42
1.5: *Processed seismic reflection profile VT-3*.....43
1.6: *A map of the study region shwoing the magnetic gradient and imaged faults*.....44

Chapter 2:
2.1: *The seismic network used for the monitoring experiment* 45
2.2: *A diagram illustrating the rotation of horizontal station components*.....46
2.3: *A flow chart outlining the processing steps carried out for each station record*.....47
2.4: *A diagram comparing raw data and processed data*.....48
2.5A: *Processed 3-component station record (MTBA) with interpreted wave phases*.....49
2.5B: *Another example (MTBA) with wave phases and a large converted phase*.....49
2.6: *A diagram showing the convention of picking a wave phase*.....50

Chapter 3:
3.1: *A diagram showing the 1-D velocity model*.....51
3.2A: *Hypocenter locations with Hypoellipse*.....52
3.2B: *Hypocenter locations with Hypoellipse: a different perspective*.....53
3.3A: *Hypocenter locations with HypoDD*.....54
3.3B: *Hypocenter locations with HypoDD: a different perspective*.....55
3.4: *A diagram summarizing the definition of strike, dip, and rake*.....56
3.5: *A comparison of hypocenter locations from two seismic networks*.....57

Chapter 4:
4.1: *A diagram summarizing the double-couple force system*.....58
4.2: *A diagram of determining focal mechanisms from P-wave first motions*.....59
4.3: *A diagram showing the beachball diagrams for the 3 fundamental fault types*.....60
4.4: *Comparison of focal mechanism solutions derived from different data types*.....61
4.5: *Focal mechanism solutions and constraint tests for an event in the dataset*.....62
4.6: *The distribution of the 66 well-constrained focal mechanisms*.....63
4.7A-E: *The focal mechanisms plotted with the events relocated using HypoDD*.....64

List of Tables

Table 1: Network information.....67
Table 2: Polarity conventions for each phase.....67
Table 3: Ph2dt parameters.....67
Table 4: HypoDD parameters.....68
Table 5: Focmec parameters.....68
Table 6: Rating system.....68
Table 7: Summary of Focal Mechanism Results.....69

List of Abbreviations

km: kilometers

Hz: Hertz

SGR: South Georgia Rift

M_w: Moment Magnitude; A measure of earthquake size, based on the static seismic moment of an earthquake.

MMI: Modified Mercalli Intensity; A measure of earthquake size, based on shaking and damage.

M_d: Duration Magnitude; A measure of earthquake size, based on the duration of an earthquake, correlated with $mb_{(Lg)}$.

$m_{b(Lg)}$: Body Wave Magnitude based on the Lg phase; a measure of earthquake size, designed to be numerically identical with the teleseismic m_b scale. This measure is commonly used for earthquakes in the central and eastern U.S recorded at regional distance.

P: Primary wave.

S: Secondary or Shear wave.

SH: Horizontal component of the shear wave.

SV: Vertical component of the shear wave.

Vp/Vs: The ratio of P wave velocity (Vp) to S wave velocity (Vs).

SEH: Standard Horizontal Error; confidence limit in the least-constrained horizontal direction.

SEZ: Standard Vertical Error; confidence limit in the vertical direction (depth).

RMS: Root Mean Square.

SVD: Singular Value Decomposition; A weighted least squares inversion method.

LSQR: conjugate gradients method; A weighted least-squares inversion method.

SEUSSN: South Eastern United States Seismic Network.

Chapter 1: Introduction

1.1: The 1886 Charleston, South Carolina Earthquake

At 9:51 PM local time on August 31, 1886 a major earthquake occurred beneath the then small village of Summerville, South Carolina. It is one of the largest earthquakes to occur on the East Coast of North America, with recent moment magnitude (M_w) estimates in the range 6.4 to 7.3 (Johnston, 1995; Bakun and Hopper, 2004). It is by far the worst earthquake disaster to have occurred on the eastern seaboard of the United States. Damage in the epicentral area reached X on the Modified Mercalli Intensity (MMI) scale (Bollinger, 1977). A value of MMI X represents severe damage and extreme shaking (Figure 1.1). Serious damage occurred in Charleston, South Carolina approximately 30 km from the epicenter where at least 83 people were killed either directly or indirectly as a result of injury and exposure (Dutton, 1889). A contoured map of the MMI from this earthquake shows the extent of the reports of felt shaking (Bollinger, 1977) (Figure 1.2).

Prior to the 1906 San Francisco earthquake, the Charleston event was the most significant earthquake disaster in the United States. This earthquake occurred in a period of time in which earthquake seismology was still a young science and no seismographic recordings were available; therefore the existing data were derived from observations of damage to structures and ground failure, such as liquefaction and lateral spreading, as well as personal accounts from people that experienced the earthquake. These observations were compiled in the 9th annual report of the USGS by Captain Clarence Dutton (Dutton, 1889). The earthquake occurred in the Atlantic coastal plain, where sediments are approximately one km in thickness. No conclusive evidence for faulting was observed in 1886. The geologic cause of the earthquake remains a matter of debate, and is the subject of this thesis.

1.2: Overview of studies related to the 1886 Earthquake

This section provides a brief overview of the previously proposed source mechanisms of the 1886 earthquake. The earliest interpretation is based on the shaking effects observed mostly along three railroads and was put forth soon after the earthquake by Clarence Dutton and a local geologist, Earle Sloan. Both Dutton and Sloan interpreted the main shock to have multiple epicenters (Dutton, 1889). In the years following the publication of the Dutton (1889) report, many researchers have attempted to build on this interpretation and propose fault models for the region. Taber (1914) studied the intensity data near Summerville and proposed a northeast-trending fault source of the 1886 earthquake that he referred to as the Woodstock Fault. USGS professional papers compiled the results of various studies undertaken by many researchers (Rankin, 1977; Gohn, 1983). Tarr (1977) suggested that the earthquakes detected near Summerville by a permanent seismic network installed in 1974 were closely associated with the rupture of the main shock. Long and Champion (1977) suggested that the shock was the result of local stress amplification. Seismic reflection profiles collected in the 1970's and early 1980's revealed several minor Cenozoic faults with reverse slip sense that could be associated with the local seismicity and the 1886 earthquake (Hamilton et al., 1983; Yantis et al., 1983; Chapman and Beale, 2008; 2010). A series of papers by Madabhushi and Talwani (1993), Dura-Gomez (2004), Dura-Gomez and Talwani, (2009) developed a fault model based largely on hypocenter locations of earthquakes occurring between 1974 and 2004. That model consists of a proposed Southwest-striking, Northwest dipping strike-slip fault (Woodstock fault), approximately 50 kilometers in length, with a compressional step-over (Sawmill Branch fault) near Middleton Place (Figure 1.3). Chapman and Beale (2008; 2010) reprocessed seismic profiles and modeled the

potential field. Their work indicates that the crust between 1 and 5 km depth in the epicentral area of the 1886 shock is comprised largely of mafic material, and discovered that the modern instrumentally located seismicity is in close proximity to at least four imaged faults that represent Cenozoic compressional reactivation of early Mesozoic extensional faults at shallow crustal depths (Figure 1.6).

1.3: Tectonic setting

The epicentral region of the 1886 earthquake is located within a large extensional terrain referred to as the South Georgia Rift (SGR) or the South Georgia Basin. This terrane was associated with the initial rifting of the supercontinent Pangaea that led to the formation of the Gulf of Mexico and the Atlantic Ocean beginning in the Triassic period. The region is overlain by Atlantic Coastal Plain sediments. Previous studies indicate that the lithology of the terrane is characterized by mafic volcanics, largely basalt, and clastic red-bed sediments similar to those found in exposed Triassic basins in the Appalachian region (Gohn 1983, McBride 1991). The geologic structure of the SGR is not well resolved, but potential field modeling done by Chapman and Beale (2010) indicates that the mafic material extends to at least four km depth in the Summerville area.

In addition to potential field modeling, there are also several wells within the region. Three wells near Clubhouse Crossroads, located a few kilometers southwest of Summerville (Figure 1.4), all encountered basalt immediately below Cretaceous coastal plain sediments. Only one out of the three Clubhouse Crossroads wells penetrated through the basalt layer, and it bottomed within a package of sedimentary red beds at a depth of 1,140 m (Gohn, 1983). An exploratory well near Lodge, South Carolina, about 70 km west of Summerville (Figure 1.4), penetrated alternating layers

of mafic volcanics and sediments and bottomed out in basalt at 3.8 km (Talwani, 2000). From these data, it is inferred that the lithology and structure of the SGR is complex and that the sequence of early Mesozoic mafic volcanics and clastic sediments is locally several kilometers thick, particularly in the Summerville area.

Seismic reflection profiles, collected in the late 1970's and early 1980's by the United States Geological Survey (USGS), the Consortium for Continental Reflection Profiling (COCORP), and Virginia Tech (VT) reveal much about the localized tectonic setting of the epicentral region. The seismic lines are shown with respect to the local county lines and rivers (Figure 1.4). There are several prominent bright reflectors seen in the lines, which represent a change in seismic impedance. Impedance is a seismic property, related to both the density of the rock and the seismic wave velocity. Changes in seismic impedance are due to compositional differences of the lithology in the subsurface. The most prominent reflectors are labeled K, J, and B (Figure 1.5). The B reflector was originally interpreted as the top of crystalline basement (Hamilton et al., 1983), but with the evidence from gravity and magnetic modeling (Chapman and Beale, 2010), and the Lodge well, it has since been reinterpreted as a basalt layer (Chapman and Beale, 2010). The J reflector is interpreted to be an unconformable contact between the early Jurassic basalt and red beds and the Cretaceous Atlantic coastal plain sediments that overly it. This reflector is strong in some profiles, particularly in line VT-3b, and weak in others. Near Clubhouse crossroads, the J reflector is clearly due to the basalt unit encountered in wells at the base of the coastal plain sediments. The J reflector changes character in different parts of the study area, and appears to be missing altogether in some places (Buckner, 2011), but it has been explained as locally homogenous material, in some places yielding a weak seismic impedance contrast (Chapman and Beale, 2008; 2010).

The K reflector is interpreted as the contact between Cretaceous and Cenozoic coastal plain sediments.

The seismic profiles obtained in the SGR reveal a complex system of extensional structures in the region (McBride, 1991). In the study area near Summerville, the B reflections show down-to-the-east offset consistent with extensional faulting; however the reflection profiles also show evidence of Cenozoic compressional reactivation of these faults. Cenozoic offset is most prominently seen in line VT-3b (Figure 1.5), as minor offset of the J and shallower reflectors. Evidence of Cenozoic faulting on other reflection profiles consists of monocline folding of the Cenozoic sediments above early Mesozoic fault offsets. Evidence for this faulting is also seen in the magnetic modeling by a steep magnetic gradient of the total intensity magnetic field. The seismic reflection profiles that pass over this gradient all exhibit Cenozoic deformation at that location (Figure 1.6).

1.4: Modern seismicity in South Carolina

The record of historical seismicity near Charleston and Summerville suggests activity both prior to and after the 1886 earthquake (Rankin 1977; Bollinger and Visvanathan, 1977). Paleo-liquefaction data indicates that several events, similar in magnitude to the 1886 earthquake, have occurred with an approximate recurrence rate of 500-600 years (Talwani and Schaeffer, 2001). Rankin (1977) suggested that recent seismicity represents aftershocks from the 1886 earthquake or events associated with the activation of closely related structures due to the change in the stress field caused by the 1886 shock. The complete historical catalog of earthquakes for South Carolina, beginning in 1698, has been compiled from a variety of sources. The events prior to the 1886 earthquake have been compiled into the catalog primarily from newspapers

and public observation reports (Bollinger and Visvanathan, 1977). Since the 1886 earthquake, many efforts have been made to improve and update this catalog.

In 1914, six earthquakes were recorded near Charleston, as well as two in the Piedmont region of South Carolina. MMI values were estimated for these earthquakes, and ranged between II and V (Taber, 1915). In 1973, a seismic network of 10 stations was installed in the region in an effort to monitor the regional seismicity. Between May 1974 and December 1975, approximately 75 earthquakes were detected, with duration magnitudes (M_d) ranging between 1.5 and 3.8 (Tarr, 1977). The catalog was updated by Tarr and Rhea (1983), compiling the events detected between March 1973 and December 1979 with a larger seismic network consisting of 21 stations. During this time, approximately 60 events were recorded, with M_d ranging from 0.6 to 3.8; the majority of the events were located near Summerville. Beginning in 1974, a permanent seismic network has been deployed near Summerville, South Carolina, and is currently operated by the University of South Carolina.

1.5: Implications of seismicity

The historical seismic record indicates that the study area is one of the more seismically active regions in the eastern United States. An earthquake comparable to the 1886 earthquake would be catastrophic. Wong et al. (2005) conducted a comprehensive earthquake loss assessment for South Carolina, using $M_w = 7.3$ earthquake near Summerville as the seismic source. They used federal government loss estimation software known as HAZUS 99, to estimate the spatial extent and scope of structural damage, casualties, and economic loss for the earthquake scenario. The results indicated that there would be approximately 45,000 casualties, 900 of

which would be fatalities. Extensive structural damage would result in losses of over 14 billion USD (estimate in 2000).

The results of Wong et al. (2005) also indicate that a significant percentage of the state's lifelines, such as hospitals and fire stations, would have moderate to severe damage. Recovery efforts would also be hindered, due to severe damage of approximately 800 bridges. It is noted that there were several uncertainties in the parameters used to determine the losses, particularly with the ground shaking estimates; however, the results still shed light on the severity of the potential earthquake risk, as well as emphasizing the need for risk mitigation. Understanding the seismicity of the region is essential for better-constrained estimates of the ground shaking associated with regional seismic events, which are crucial for the on-going earthquake risk mitigation efforts in South Carolina.

1.6: Project overview

The purpose of this study is to shed more light on the modern seismicity near Summerville, to determine the likely fault(s) associated with the earthquake, and develop a testable hypothesis for the geologic process driving the 1886 earthquake. The study involves analysis of data collected in a one-year seismic monitoring experiment. The results of the data analysis are accurate hypocenter locations and well-constrained focal mechanism solutions, which have implications for the causal fault structure and state of stress associated with the 1886 earthquake.

Chapter 2. Data Processing and Methods

2.1: Data set and station network overview

From August 7, 2011 to August 30, 2012, a network of eight temporary stations funded by the USGS (under award number: G11AP20141: "Experiment to Determine Hypocenters and Focal Mechanisms of Earthquakes Occurring in Association with Imaged Faults near Summerville, South Carolina") were deployed near Summerville, South Carolina (Figure 2.1; Table 1) to continuously record local seismicity (Chapman and Beale, 2013). Data were recorded using 3-component, short period, 2 Hz seismometers (Sercel L-22) on high-resolution digital data recorders (REF TEK 130), loaned by the IRIS/PASSCAL instrument center at the New Mexico Institute of Mining and Technology in Soccoro, New Mexico. The stations were equipped with solar panels to provide power to 12-volt marine storage batteries and GPS receivers for location and timing. The data were collected with a sample rate of 100 samples/second. The data are archived at the IRIS Data Center under the 'XY' seismic network code, and are available to the research community from the IRIS data management center. In addition to the temporary deployment, 3 permanent seismic stations supported by the ANSS (Advanced National Seismic System under the USGS) and operated by the University of South Carolina collected data for the duration of the experiment (Figure 2.1; Table 1).

2.2: Processing steps

Most of the processing was conducted using the Seismic Analysis Code (SAC) software package (Goldstein and Snoke, 2005). Through an automated process, the program read in the data for a given station, synchronized the record start time on all three components, removed a linear trend, and applied a Butterworth bandpass filter

with 3 poles and corner frequencies at 1 and 40 Hz (Figure 2.3). The bandwidth of the Butterworth filter was less broad for station NHSC (with corner frequencies at 1 and 15 Hz), because of the low Nyquist frequency (20 Hz) for that station. Synchronizing the data ensures that the signal of all three components begins at the same reference time. Removing the trend is a signal correction command that eliminates potential signal slope artifacts when integrating the record; it also effectively removes the mean amplitude from the data. The Butterworth bandpass filter preserves the signal amplitude between the two corner frequencies while the remaining frequencies are reduced in amplitude.

Each recorded component was integrated from the raw signal (proportional to ground velocity at frequencies greater than 2 Hz) to approximate the single-sided displacement pulses at the source, thus simplifying the measurement of P and S wave arrival amplitudes. An ideal displacement phase arrival (either P or S wave) would consist of a single-sided waveform, in a homogeneous whole space. Integrating the recorded trace from the 2-Hz velocity sensors used in this study gives a good approximation to this signal for the small magnitude events of the study region.

An essential step in the data processing was the rotation of the horizontal components to the radial and transverse directions. This rotation was performed for two reasons: 1) To allow accurate S wave arrival time picking from the transverse component, and 2) to isolate the SV and SH components of the S wave for amplitude measurement. This step in the processing required an initial estimate of the hypocenter location in order to determine the source-receiver azimuth needed to establish the radial and transverse component directions.

Over the course of the monitoring experiment, 134 locatable earthquakes were identified in the data set. P and S-wave arrival times were picked on the un-rotated

components and the hypocenters were initially located individually using the computer program Hypoellipse (Lahr, 1999). Given the source-receiver azimuth estimates from the initial location, the rotation of the North-South and East-West components to transverse and radial horizontal components was done using Equation 1, implemented by SAC (Figure 2.2).

$$\begin{bmatrix} R \\ T \end{bmatrix} = M_{2D} \begin{bmatrix} N \\ E \end{bmatrix} \quad ; \quad M_{2D} = \begin{bmatrix} \cos(a) & \sin(a) \\ -\sin(a) & \cos(a) \end{bmatrix} . \qquad (1)$$

The variable, a, represents the azimuth measured clockwise from North, which was determined in the initial Hypoellipse location. Two permanent stations (CSB and RGR) have been installed in boreholes with undetermined orientation of the horizontal components. As a consequence, rotation was not implemented for CSB and RGR, and SV and SH polarity and amplitude measurements could not be made for those stations.

Following the initial location of the hypocenters, and creation of transverse and radial components of motion, a coda duration magnitude for each event was calculated using Equation 2, developed by the Virginia Tech Seismic Observatory, which is calibrated to the body wave magnitude scale ($m_{b(Lg)}$). Several network operators in the southeastern United States have used this duration magnitude since the early 1980's (M. C. Chapman, personal communication).

$$M_D = -3.42+2.83 \text{ Log } D \qquad (2)$$

The duration magnitudes of the earthquakes ranged from -1.8 to 2.6. Figure 2.4 shows a comparison of unprocessed versus processed seismograms. After processing, the signal to noise ratio was improved, and the P and S-wave arrivals appear more impulsive and easier to distinguish.

2.3: Picking phase arrival times, polarities, and amplitudes

After the processing described above, the data were extensively analyzed to identify and measure body wave arrival times, polarities and amplitudes: the P wave on the vertical component, the SH component of the S wave on the transverse component, and the SV component of S wave on the radial component. Figure 2.5a shows an example seismogram from the dataset, with the interpreted arrival times for each phase. Noise and the presence of converted energy complicated this process. In a general sense, converted waves result from scattering due to velocity and density heterogeneities in the Earth (M. C. Chapman, personal communication). This scattered energy is present in the seismograms, in addition to the direct P and S arrivals, making it more difficult to interpret the direct P and S arrivals. Conversion of SV to P waves was a particular problem for the radial component. The S to P converted phase due to the velocity contrast at the base of the coastal plain sedimentary section can have large amplitudes on the vertical and radial components. Figure 2.5b shows an example from the data set where the converted phase is very prominent. This phase can easily be mistaken for the SV arrival, and it takes an experienced eye and 3-component data to distinguish the two. S to P conversion at other points along the raypath can also generate precursory arrivals that further complicate the measurement of SV arrival time and amplitude. For this reason, the SH arrival times derived from the transverse components were used to establish the S wave arrival times necessary for final hypocenter location. A weight, ranging between 0 and 4 was assigned to each P and S arrival time to characterize the quality and uncertainty associated with the picks. In Hypoellipse, a weight of 0 is assigned to a phase arrival if it is fairly impulsive and easy to distinguish from surrounding noise, while a weight of 4 is assigned if there is no discernable wave phase arrival in the

record. In practice, arrivals were assigned with weights of 0, 2, and 4 for consistency. Weighting is an integral part of picking P and S arrival times, as it is used in part to determine the uncertainty of earthquake locations (Chapter 3).

In addition to the arrival times, the polarity and amplitude of each direct body wave phase was picked using the first half-cycle of motion following the arrival onset, and were recorded using SAC (Figure 2.6). P-wave arrival times, polarities and amplitudes were determined using the vertical component. S wave arrival time, SH polarities and amplitudes were determined using the transverse horizontal component. SV polarities and amplitudes were determined from the radial horizontal component. The naming convention for P wave polarity is U or D for either first motion in the up or down direction. The SH polarity naming convention is R or L, corresponding to first motion to the right or left, when looking in the direction of source-to-receiver azimuth. The convention for SV is F or B, representing either forward (horizontal motion away from the source) or backward (horizontal motion toward the source) along the source-to-receiver azimuth (Table 2). The phase amplitudes corresponded to either the amplitude of the first peak or trough following the phase arrival time, measured in digital counts on the integrated seismograms.

Chapter 3. Determining hypocenters

3.1: Locating hypocenters using Hypoellipse

All events in the data set were initially located using a computer program called Hypoellipse (Lahr, 1999). Hypoellipse determines the hypocenter of regional earthquakes. The hypocenter is the location at depth of earthquake rupture initiation, whereas the epicenter is the projection of the hypocenter on the surface of the Earth. Hypoellipse uses Geiger's method for earthquake location, which involves the linearization of a nonlinear problem, as the relationship between P and S arrival times and the spatial location of an earthquake, is nonlinear (Lahr, 1999; Waldhauser, 2001). The resultant linear relationship relates travel-time residuals to perturbations in a given earthquake location model containing spatial and temporal parameters (Waldhauser and Ellsworth, 2000).

Hypoellipse implements the weighted Least Squares inversion method to effectively minimize the root mean square (RMS) of the residual of observed and calculated travel-times from source to station through an iterative process (Lee and Dodge, 2010). A solution for the location model is achieved after several iterations, containing spatial x-y-z coordinates of the source and a source origin time, as the RMS of the travel-time residual is minimized to a reasonable user-defined value. Equation 3 shows the equation for the travel-time residual below, where the observed travel-time is known through the P and S arrival times and the calculated travel-time is theoretical and based upon the velocity model used for the region. Equation 4 shows the root mean square residual for iterations 1 through N, where i is a given iteration, and W is the weight computed by Hypoellipse for the i'th iteration (Lahr, 1999).

$$r_i = (\tau^{obs} - \tau^{calc}) \quad (3)$$

$$RMS = \sqrt{\frac{\sum_{1}^{n} W_i r_i^2}{\sum_{1}^{N} W_i}} \quad (4)$$

Several parameters must be defined to control the execution of Hypoellipse. Most of these parameters control the weighting of the data as iteration progresses. The fundamental user-provided inputs to the program are the phase arrival times, seismic station locations and an appropriate 1-dimensional velocity model. The user can also provide initial estimates of the hypocenter and/or origin time. The P and S arrival times were measured from the seismograms collected in the study area (see Chapter 2). The velocity model is needed to determine the theoretical travel times, used to calculate the residual in equation 3. A velocity model previously determined consisting of three layers over a half-space, was used for this analysis (Chapman et al., 2003). The velocity model (Figure 3.1) incorporated a shallow layer representative of the Cretaceous and younger coastal plain sediments, with P and S wave velocities 2000 km/s and 0.667 km/s respectively. The second layer contained higher P and S wave velocities of 6000 km/s and 3.468 km/s respectively, representative of the lower Mesozoic volcanic and sedimentary rock section. The third layer, representative of the deeper crust contained somewhat higher P and S wave velocities, 6.5 km/s and 3.757 km/s respectively, that were determined from refraction velocity measurements in the Piedmont province of Virginia (Bollinger et al., 1980). Due to the small epicentral distances involved in this study, only the two shallowest layers are important.

134 earthquakes in total were located using Hypoellipse, and the resultant hypocenters are shown in both map view and in two perspective views (Figure

3.2a,b). When looking along an approximate East-West cross-section slice, the hypocenters appear to define a tabular zone trending approximately North-South and dipping towards the west. The implications of this result will be discussed further in Chapter 5.

For each hypocenter, Hypoellipse also determines a 68% confidence limits of the location, defined by SEH and SEZ, the horizontal and vertical semi-major axes of an ellipsoid representing the confidence limit in the least well-constrained horizontal direction and the confidence limit at depth, respectively (Lahr, 1999). These errors are based upon an estimated standard error of arrival times calculated by the program, the weight code assigned to each arrival time, and the partial derivative of travel-time from the source to each station. The standard error of arrival times is either computed by Hypoellipse, on the basis of the RMS residual or set by the user at an appropriate fixed value. In the case of small data sets, significant uncertainties in the locations of the hypocenters can result from arrival time reading the errors and poor spatial constraint. In addition, uncertainties in the velocity model can lead to bias in the locations. Under the right conditions, relative location methods can be used to greatly reduce the effects of error in the velocity model. This approach was used to good advantage in this study, as described below.

3.2: Re-locating hypocenters using HypoDD

Hypocenter locations are often relocated relative to each other to yield more precise relative locations. A computer program known as HypoDD implements a double-difference location algorithm, and was used to relocate the earthquake hypocenters determined by Hypoellipse. Like Hypoellipse, HypoDD linearizes the nonlinear relationship between the source location and its station arrival times using

Geiger's method, but minimizes the differences in travel-time for two nearby events (Waldhauser, 2001). This residual, referred to as the double-difference, is shown in Equation 5 (Waldhauser and Ellsworth, 2000):

$$dr_k^{ij} = (t_k^i - t_k^j)^{obs} - (t_k^i - t_k^j)^{calc} \quad (5)$$

The index notation is the same as in equation 3, with the addition of index j, which represents the second event in the earthquake pair. HypoDD gives the option of minimizing the residuals by weighted least squares with either the Singular Value Decomposition (SVD) method or by the conjugate gradients (LSQR) method (Waldhauser, 2001). Both methods have their advantages, based on the goal and parameters of a given study, but in general SVD is more appropriate for well-conditioned and smaller clusters of events and the LSQR method is able to efficiently solve large and potentially ill-conditioned systems (Waldhauser, 2001). While the size of this dataset is more appropriate for SVD, the LSQR inversion method was used based on the uncertainty of the condition, due to sparse station coverage. It is noted that in future work, SVD should be used to invert for the model solution to be compared with results using LSQR.

As a further constraint, HypoDD allows multiple data input sources to be used by the program; these include traditional arrival time catalogs comprised of traditional arrival time picks as described in section 2.3, and/or high precision relative arrival times determined from cross-correlation waveform data (Waldhauser, 2001). For this study, the input data source included only catalog data (manual P and S wave arrival measurements). Waveform cross correlation can provide more accurate relative arrival time measurements in many cases. However, tests have shown that the small hypocenter distances and high frequency content seismograms used in this study

make for manual arrival time picking accuracy of the same order as that from waveform cross-correlation.

The first step for earthquake relocation using HypoDD involves data preparation, performed by a program named ph2dt. The purpose of this program is to search the catalog data and/or waveform data and link neighboring earthquakes into a pair and calculate the double-difference for the pair (Waldhauser, 2001). There are several parameters involved in running this program, which can be altered appropriately, depending on the dataset. These include the maximum event separation for linkage, the range of double-difference observations, the maximum amount of neighboring events, the minimum amount of links for each event, and the maximum distance between hypocenters, which defines the size of the earthquake cluster. The parameter values were chosen based on appropriate values for a relatively small event cluster given by the HypoDD manual (Waldhauser, 2001), and are summarized in Table 4. In this step, it is possible that events get "thrown out" of the dataset, if they are defined as outliers to the dataset. Outliers are defined as events containing delay times that are larger than the maximum expected delay time for a P and S wave to travel between two events in an event pair. In this study, 47 events were thrown out, leaving 87 to be relocated.

In the second and final step for earthquake relocation, HypoDD is run to determine the double-difference hypocenter locations in an iterative process. After each iteration, the vector difference between nearby hypocenter pairs is adjusted, the model parameters are updated, and the dataset is weighted based on the data misfit from inversion. The number of iterations is dependent on the inversion parameters and the amount of uncertainty within the dataset. A solution is found once the shifts in hypocenter locations are within the average error of the initial locations or when the

RMS residual is minimized to below the threshold of noise in the dataset (Waldhauser, 2001). Many parameters are involved in HypoDD, including the 1-D velocity model, the Vp/Vs ratio, and the maximum distance between hypocenters. As with ph2dt, these parameters were also tested with several values to assess their control on the hypocenter locations, particularly the depths. The only parameter that affected the depths significantly was altering the Vp/Vs ratio, which illuminates a major limitation in HypoDD. Only one Vp/Vs ratio can be specified for the entire velocity model, which is not appropriate for the near-surface depths involved in this study. In Fall 2014, a new version of HypoDD will become available to correct this limitation, and future work should include multiple Vp/Vs ratios to test the constraint on the hypocenter depths. The parameters used for HypoDD are summarized in Table 5.

Out of the 134 events, 87 were relocated, and the results are plotted in both map view and in perspective views in Figure 3.3. When compared to the initial locations performed by Hypoellipse, the HypoDD algorithm was successful in tightening the clusters of events, making them more precise. They exhibit the same North-South trending, west-dipping seismogenic feature observed in the Hypoellipse locations.

3.3: Plotting and analysis of hypocenters

HypoDD outputs the event re-locations in the format of latitude, longitude, and depth. Latitude and longitude are used to plot the hypocenters in map view as epicenters. Viewing hypocenters in perspective plots is advantageous for determining any geometric trends: e.g., a planar arrangement of hypocenters might represent a fault. In order to plot them in a perspective view, a reference origin in Cartesian coordinates (x, y, z) must be determined, as latitude and longitude cannot be used. It is

noted here that z is equal to the depth and remains unchanged. The origin of the x-y coordinate systems is referenced to the mean latitude and longitude of the earthquake epicenters. Equations 6-8 were used to determine the Cartesian x and y coordinates of the hypocenters relative to the origin (Bullen and Bolt, 1985):

$$\cos\Delta = A A' + B B' + CC' \quad , \tag{6}$$

$$A = \sin\theta \cos\phi, B = \sin\theta \sin\phi, C = \cos\theta, D = \sin\phi, E = -\cos\phi \tag{7}$$

$$2 + 2 \sin\Delta \sin Z = (A' - D)^2 + (B' - E)^2 + C'^2 \quad , \tag{8}$$

The variables θ and ϕ represent the mean colatitude and mean longitude of the epicenter cluster, respectively, and θ' and ϕ' are the colatitude and longitude of a given event epicenter, respectively. The angular epicentral distance, between the origin and epicenter in degrees subtended at the center of a sphere is represented by Δ, and Z is the azimuth from origin to epicenter in degrees, reckoned East of North. Cartesian coordinates, x and y in kilometers, with respect to the origin are given by Equation 3.7.

$$x = 111.199\,\Delta \sin Z, \quad y = 111.199\,\Delta \cos Z \quad . \tag{9}$$

The HypoDD relocated hypocenters appear consistent with the hypocenters located with Hypoellipse. In a geologic sense, the orientation of a plane, or a fault, is defined by a strike and a dip. The strike is defined as the azimuth of a line that marks the intersection of a given plane with a reference horizontal plane, and the dip is the acute angle between the plane and the horizontal: positive dip direction is reckoned to the right when looking in the strike direction (Figure 3.4). A plane was fit to the hypocenters by weighted least squares for the purpose of quantifying the orientation of the feature. Hypocenters at depths greater than 7 km were given four times the weight of the remaining hypocenters. The orientation of the best-fit plane to the

hypocenter locations was found to be striking N186E and dipping 43 degrees to the west. Two additional planes were fit to the HypoDD hypocenter data: 1) with equal weighting of all events and 2) excluding all hypocenters at depth greater than 7.0 km. Equal weighting of all events resulted in a least-squares strike of N185E and a dip of 34 degrees, while the exclusion of deeper hypocenters resulted in a strike of N184E and a dip of 18 degrees. The resultant orientations for the planes included significantly shallower dips, but the strike of both scenarios was relatively unchanged (N185E).

3.4: Discussion and implications of results

The 134 hypocenters located with Hypoellipse illuminate a distinct North-South trending, west-dipping seismogenic zone when viewed in a perspective plot looking towards the North (Figure 3.2a). HypoDD relocated 87 of the hypocenters, and they show more consistent and precise relative locations, compared to the Hypoellipse locations (Figure 3.3a). Most of the events are located within the upper 6 km, and there is a noticeable gap in the trend at a depth of around 8 km. The events below 8 km are assumed to be significant in conjunction with focal mechanism solution results (Chapter 4).

The hypocenters discussed above were compared to hypocenters computed for earthquakes that occurred from 1974-2005. The arrival time data for those earlier earthquakes were contributed to the Southeastern United States Seismic Network Bulletins (e.g., Chapman et al., 2006) by Dr. Pradeep Talwani and co-workers at the University of South Carolina. Those earlier earthquakes were re-located by Jake Beale and Qimin Wu using the procedure described in detail in the previous sections. The results indicate good agreement between the two datasets in terms of the plane

orientation (Figure 3.5). This is a significant result, as it shows that the hypocenter results from a one-year monitoring experiment are representative of the longer-term seismicity during the past 3 decades.

Chapter 4. Determining focal mechanisms

4.1: Source characterization using focal mechanisms

A common practice associated with analyzing the seismicity of a region is to determine the focal mechanism for earthquakes in conjunction with locating hypocenters. The focal mechanism of a tectonic earthquake is assumed to be represented by two orthogonal force systems, known as a double couple (Figure 4.1). The general seismic source is characterized by a seismic moment tensor, in which the tensor elements represent force couples acting at a point in a continuum. The double couple is a subset of general seismic moment tensors that represents the force system responsible for shear dislocation on a plane. It is assumed here that moment tensors of all the events are pure double couple (Lay, T. and Wallace, T., 1995). In future work, it would be interesting to derive the general seismic moment tensor, but such work is beyond the scope of the present study. The double couple focal mechanism can be described by static moment (or moment magnitude), the strike and dip of the two nodal planes, and the rake (direction of slip) on the nodal planes. Because of symmetry, there are two orthogonal nodal planes, either of which could correspond to the actual fault plane. Determination of which of the two nodal planes is the actual fault plane requires information in addition to recordings of the far-field seismic waves. The additional information is usually, as here, furnished by the hypocenter locations of aftershocks, or in some cases, by geodetic data or by surface rupture.

The standard lower hemisphere stereographic projection of the two nodal planes is used here to illustrate all focal mechanism solutions. It is constructed with the orientation of a fault in terms of strike, dip, and rake (Figure 3.4). The rake angle refers to the direction of slip of the hanging wall of a fault, with respect to the foot wall. It is reckoned as counterclockwise from the strike direction in the plane of the

fault. The focal mechanism solution plot is commonly referred to as a beach ball diagram, where the strike, dip, and rake define the quadrants of the projection. There are also three axes, plotted as points, that represent the pressure (P), the tensional (T) axis, and the null axis (N), which marks the intersection of the two nodal planes (e.g., fault plane and the auxiliary plane). In some studies, a B represents the notation for the null axis. In this study, the latter will be referred to as the null axis.

The double couple source generates a characteristic radiation pattern for P, SV and SH waves. Amplitudes and polarities are functions of fault strike, dip and rake as well as the source-to-station azimuth and ray take-off angle at the source. Thus, the strike, dip and rake of both nodal planes can be inferred from P and S wave polarity and amplitude data given recordings at several stations surrounding the epicenter. For example, if the P wave first motion polarity is recorded for several seismic station records, they can be plotted on the stereographic projection as either compressional (P wave polarity is up and horizontally away from the source) or dilatational (P wave polarity is down and horizontally toward the source). With many first motions plotted on the stereographic projection, compressional and dilatational quadrants can be defined by two great circles, representing the fault plane solution and the auxiliary plane (Figure 4.2). The SV and SH waves exhibit different radiation patterns. Together, the polarities of the P, SV and SH waves and their amplitudes provide the data necessary to determine the focal mechanism. Without additional geologic or seismic data, the fault plane cannot be distinguished from the auxiliary plane, but it can still provide a check on the consistency with the orientation of the seismogenic zone illuminated by the hypocenter locations. By convention the P wave compressional quadrants are shaded in the beachball diagrams. Focal mechanism solutions for the three fundamental types of faults are shown in Figure 4.3.

4.2: Determining focal mechanisms using Focmec

Focmec is a program, written in Fortran-77, that solves for all possible focal mechanism solutions that fit within criteria, based on the data set and the specified threshold for allowed error (Snoke, 2003). The data input include polarities of P, SH, and SV wave phases, and SH/P and SV/P amplitude ratios of each station for each event. The use of P, SH and SV amplitudes requires that the measurements be corrected to represent those at the source. This correction involves the computation of amplitude changes at major impedance contrasts within the Earth model, and at the free surface. For this study, this required correction for the impedance contrast at the base of the coastal plain sediments and free surface effects for P, SV, SH. These corrections were performed using a Fortran program derived by Martin Chapman. The program traces the P and S wave through the velocity structure and computes the amplitude change at each impedance contrast and at the free surface (Martin Chapman, personal communication).

In addition to accounting for impedance contrasts and the free-surface effect between the source and receiver, Focmec requires the specification of parameters that control the constraint of the solution (Table 6); these include the number of allowed polarity errors and amplitude ratio errors. A polarity error is defined by the uncertainty associated with picking the first motion polarity of the wave phase. An amplitude ratio error is defined by a value that falls outside the specified range of deviation between the calculated and observed amplitude ratios (Snoke, 2003). The number of allowed polarity and amplitude ratio errors can be adjusted iteratively to achieve the best-constrained solution with the minimum amount of allowed errors. The amount of allowed errors was different for each event examined here and dependent on the quality of the station records. As discussed in Chapter 2, it was sometimes difficult to

pick phase polarities and amplitudes due to significant noise present in the record; therefore, a level of uncertainty is expected to be conveyed through the constraint of the focal mechanism solutions. Focal mechanism solutions were generated for all 134 events and underwent a detailed analysis to test the constraint of the solutions.

4.3: Constraint testing

Focmec performs a grid search over all possible fault strike, dip and rake angles. The degree of constraint on a fault plane solution is reflected by the diversity of possible mechanisms that fit the data, with a minimum of polarity and amplitude errors. Previous studies have shown that including first motion polarities of SH and SV wave phases in addition to P waves (as mentioned in the previous section) result in improved constraint (Snoke, 2003). Additional constraint is provided by using amplitude ratio data in addition to using first motions polarities (Snoke, 2003; Chapman and Beale, 2013). Figure 4.4 illustrates the difference in focal mechanism solutions when adding just one amplitude ratio in addition to polarities from first motions. This project included polarities and ratio amplitudes of all wave phases to obtain the best possible focal mechanism solutions.

The focal mechanism solutions underwent two types of constraint testing: 1) An initial constraint test involving the addition of a single allowed polarity error, and 2) a more detailed constraint test that involved running Focmec with 500 polarity errors and again with 500 amplitude ratio errors. The initial constraint test was performed for the purpose of characterizing the threshold of uncertainty of each solution. If the addition of a single error changed the solution drastically, it implies poor constraint in the solution. The second constraint test was performed to test if the solution's constraint relied more on the polarity or amplitude ratio data. Figure 4.5

shows the focal mechanism solutions for the best solution and for the constraint tests for a given event in the dataset. A subset of well-constrained focal mechanism solutions was obtained through the results of the constraint testing.

4.4: Plotting and analysis of focal mechanisms

The focal mechanisms were plotted using a subprogram of Focmec called focplt. The input data is the output file of Focmec, which lists the solutions in terms of strike, dip, and rake. The solutions are plotted on a lower hemisphere equal-area (Lambert-Schmidt) stereographic projection with many available plotting options (Snoke, 2003). In this dataset, results plotted include the fault planes, P, T, and B axes, and symbols that represent the P, SH, and SV polarities. The best solution and both constraint tests were plotted and analyzed to characterize the results in terms of orientation, slip sense, and constraint (Figure 4.5).

The 134 focal mechanism solutions were narrowed down to 73 solutions by both initial inspection, as many of the events showed inconclusive solutions, (poor constraint) in which the fault orientation and/or slip direction could not be deduced, and constraint testing mentioned above. For the 73 events, further characterization included a quality rating system based on the number of stations recording an event, the number of polarities, and the number of amplitude ratios. Analogous to a typical classroom grading system, an A rating corresponds to a well-constrained solution and an F rating corresponds to a poorly constrained solution. Table 6 summarizes the specific conditions of the number of stations, polarities, and amplitude ratios corresponding to a particular rating. In summary, 21 mechanisms received an A rating, 22 received a B rating, 23 received a C rating, and 7 received an F rating. The 7 mechanisms with an F rating were removed from the data set, and the remaining 66

mechanisms were categorized by fault orientation and slip direction. The fault plane solutions included 55 dip-slip reverse motion mechanisms and 11 strike-slip mechanisms. The large group of reverse mechanisms was subdivided based on the approximate trend of the B or null axis (or trend of the nodal planes) within a range of +/- 22.5 degrees in azimuth: 28 trending North-South, 7 trending East-West, 7 trending Northeast-Southwest, and 13 trending Northwest-Southeast (Figure 4.6). The focal mechanism results of each event were summarized, including the rating, category, number of stations, number of polarities, number of amplitude ratios, and hypocenter depths determined by both Hypoellipse and HypoDD (Table 7).

4.5: Discussion and implications of results

Out of the 66 well-constrained focal mechanisms, the dominant slip sense is dip-slip in reverse motion, including 83.3% of the mechanisms. Within the reverse mechanism category, 42.4% of them were categorized as trending approximately N-S. These results imply that a significant percentage of the focal mechanisms are consistent with the N-S trending seismogenic zone, shown in Chapter 3, which is an exciting observation. In addition, the dip-slip reverse slip sense is consistent with previously imaged Mesozoic faults identified in seismic reflection profiles (Chapman and Beale, 2008, 2010).

Chapter 5. Conclusions

A seismic network, involving 8 temporary stations, was operated near Summerville, South Carolina from August 2011 through August 2012 to shed light on the local seismicity and its association with the 1886 Charleston earthquake, as well as the proposed fault structures from previous literature (Chapman and Beale, 2008, 2010; Dura-Gomez, 2004; Dura-Gomez and Talwani, 2009). The results consisting of 134 hypocenter locations, 87 double-difference hypocenter relocations, and 66 well-constrained focal mechanism solutions reveal some interesting observations.

The hypocenter locations show a south-striking, west-dipping tabular zone. A plane striking N186E and dipping 43 degrees to the west was fit to the hypocenters relocated using HypoDD (Figure 3.3a). Most of the hypocenters are within the upper five km of the subsurface, implying that those events are occurring in the Mesozoic package of largely mafic material (Chapman and Beale, 2010). The hypocenters in this study also show good agreement with hypocenter locations of earthquakes occurring in the time period 1974-2005 (Figure 3.5), indicating long-term stationary presence of the seismicity. The re-processed reflection data of Chapman and Beale (2010) do not constrain the strike direction of the individual faults imaged in that study. The faults imaged by Chapman and Beale (2010) lie in the hanging wall of the projection of the inferred fault plane described here, if it is projected up-dip to the ground surface. The imaged faults are within and on the northwest flank of a Mesozoic extensional basin lying between Summerville and Charleston (Chapman and Beale, 2010; see Figure 1.6). The projection of the inferred west-dipping fault defined in this study is near the center of this shallow extensional basin. A direct

relationship between the faulting imaged on the reflection profiles, and the inferred South-striking fault at depth defined here is not clear at this time.

66 well-constrained focal mechanism solutions were determined using Focmec in an attempt to better-characterize the seismicity, in conjunction with the hypocenter locations. Approximately 83% of the mechanisms show primarily dip-slip, reverse motion faulting with variable P axis orientations. The dominant P axis orientation trends approximately East-West, but there is considerable variability. The variability of the focal mechanism distribution can potentially be explained by the concept of Coulomb stress transfer. Equation 10 shows that a change in Coulomb stress has two components: the shear stress change and the normal stress change. The shear stress change occurs in the direction of slip on a fault and is represented by $\Delta\tau$. The normal stress change, represented by $\Delta\sigma$, occurs orthogonal to the fault plane and is dependent on the effective coefficient of friction associated with motion of the fault plane (King et al., 1994).

$$\Delta\sigma_f = \Delta\tau + \mu' \Delta\sigma \quad . \qquad (10)$$

When slip occurs on a fault, the stress drop on the fault alters the stress field in the volume surrounding it. This alteration can result in slip on secondary faults (aftershocks) with different orientation from the initial earthquake. This may be an explanation of the variability seen in the P axes of the focal mechanisms. Similar variability is observed in the aftershock series of the 2011 Mineral Virginia earthquake. Wu et al. (2015) modeled the Coulomb stress change in the Virginia aftershock sequence, and found that between 82 and 92% of events experienced a positive stress change, indicating that the diversity of mechanisms can be largely

attributed to re-activation of faults with a wide range of orientation by the process of Coulomb stress transfer.

The hypocenters and focal mechanism solutions determined in this study point to the possibility that the persistent modern seismicity near Summerville, South Carolina is in fact a continuing aftershock sequence of the 1886 Charleston earthquake. This idea is not new, and was suggested in previous studies regarding this earthquake (Tarr, 1983; Rankin, 1977). A long-term aftershock sequence might be the result of Coulomb stress transfer from the 1886 earthquake in a low strain rate environment. Intraplate regions have, on average, strain rates that are at least 100 times smaller than plate boundary areas (M.C. Chapman, personal communication). It may be that the local perturbations to the regional stress field caused by Coulomb stress transfer in 1886 could persist for a very long period of time until the regional stress equilibrium is re-established locally. The majority of focal mechanisms are consistent with a subhorizontal maximum compressive stress trending approximately East-West, rotated only slightly from the Northeast average direction for thrust faulting in eastern North America, inferred by Zoback (1992). In this case the south-striking, west-dipping tabular zone of seismicity would be likely defining the orientation of the fault that ruptured in the 1886 earthquake, and the focal mechanism distribution of the modern seismicity represents smaller-scale structures being activated due to Coulomb stress transfer. This interpretation is based on an analogy with the 2011, Mineral Virginia earthquake. The aftershocks of the recent Virginia shock outline the orientation of the main shock rupture, but do not fall within the area of mainshock moment release (Chapman, 2013). Instead, they occur at shallower depths, further along strike and up-dip of the mainshock. Although most of the Mineral aftershocks exhibit reverse mechanisms, many of them show very different

nodal plane strikes, exhibiting a range of approximately 90 degrees in P axis trend (Wu et al. 2015). Interestingly, the Mineral aftershocks occur within a zone that exhibits the same orientation as the mainshock nodal plane. This characteristic of the Virginia shock may well apply to the seismicity near Summerville. On that basis, I advance the hypothesis that the 1886 event occurred by compressional re-activation of a south-striking west-dipping early Mesozoic extensional fault. The orientation and slip sense of the fault proposed here is very different from that of previously proposed fault models for the 1886 earthquake, particularly the Woodstock fault model (Figure 1.3). The Woodstock fault model is transpressional, with strike-slip motion on fault segments striking N30°E and dipping to the Northwest, with a reverse stepover (Dura-Gomez, 2004; Dura-Gomez and Talwani, 2009).

The limited data set from the temporary station deployment has shed some new light on the mystery concerning the geologic cause of the 1886 Charleston earthquake. The hypothesis advanced here can easily be tested by future work, with a denser station network deployed for a longer duration. A network containing at least 12 stations in addition to the permanent stations and a two-year experiment duration would likely yield a dataset double the size of that used here. Seismic data collection from properly designed local network deployments are essential for studying earthquakes (Chapman 2009). The 1886 Charleston earthquake occurred before the development of seismic instrumentation, but it appears to have left a legacy of on-going seismicity that needs to be researched. This work is needed for the assessment of the regional seismic hazard, for applications of seismic hazard mapping, and creating regulations for building codes.

References

Ackermann, H. D. (1983). “Seismic-refraction study in the area of the Charleston, South Carolina, 1886 earthquake”, *in* Studies Related to the Charleston, South Carolina, Earthquake of 1886 Tectonics and Seismicity, G. S. Gohn, Editor, United States Geological Survey Professional Paper 1313, p. F1-F20.

Bakun, W. H. and Hopper, M.G. (2004). "Magnitudes and Locations of the 1811–1812 New Madrid, Missouri, and the 1886 Charleston, South Carolina, Earthquakes." *Bulletin of the Seismological Society of America*, **94**(1). p. 64-75.

Behrendt, J. C. (1985). "Structural Interpretation of Multichannel Seismic Reflection Profiles crossing the Southeastern United States and the Adjacent Continental Margin-Decollements, Faults, Triassic(?) Basins and Moho Reflections." *Reflection Seismology: The Continental Crust*, **14**, 13 pp.

Bollinger et al. (1980). “Central Virginia seismic network: Crustal velocity structure in central and southwestern Virginia.” NUREG/CR-1217, U.S. Nuclear Regulatory Commission Contract No. NRC-04-077-134, 133 pp.

Bollinger, G. A. (1977). “Reinterpretation of the intensity data for the 1886 Charleston, South Carolina, earthquake.” *in* Studies Related to the Charleston, South Carolina, Earthquake of 1886-A, Preliminary Report. D. W. Rankin, editor, United States Geological Survey Professional Paper 1028, p. 17-32. (URL: http/pubs.usgs.gov/pp/1028/report.pdf)

Bollinger, G. A. and Visvanathan, T.R. (1977). “The seismicity of South Carolina prior to 1886.” Studies Related to the Charleston, South Carolina, Earthquake of 1886-A Preliminary Report." *in* D. W. Rankin, United States Geological Survey Professional Paper 1028, p. 33-42.

Buckner, J. (2011). “Crustal Structure in a Mesozoic Extensional Terrane: The South Georgia Rift and the Epicentral Area of the 1886 Charleston, South Carolina, Earthquake”. Department of Geosciences. Blacksburg, VA, Virginia Polytechnic Institute and State University. Master of Science. 57 pp.

Bullen, K.E. and B.A. Bolt (1984). “Introduction to the Theory of Seismology, 4th ed.”. Cambridge University Press, London. 499 pp.

Chapman, M.C. (2013). “On the Rupture Process of the 23 August 2011 Virginia Earthquake.” Bulletin of the Seismological Society of America. **103**(2A). p. 613-628.

Chapman, M.C. (2009). A Comparison of Short-Period and Broadband Seismograph Systems in the Context of the Seismology of the Eastern United States, *Seismological Research Letters,* 80, p. 936-952.

Chapman, M.C. and Beale, J.N. (2013). Experiment to Determine Hypocenters and Focal Mechanisms of Earthquakes Occurring in Association with Imaged Faults near Summerville, South Carolina, Final Technical Report to USGS External Research Program, 13 pp. URL http://earthquake.usgs.gov/research /external/research.php, last accessed December 15, 2014.

Chapman, M. C. and Beale, J.N. (2010). "On the Geologic Structure at the Epicenter of the 1886 Charleston, South Carolina, Earthquake." *Bulletin of the Seismological Society of America* **100**(3). p. 1010-1030.

Chapman, M. C. and Beale, J.N. (2008). "Mesozoic and Cenozoic Faulting Imaged at the Epicenter of the 1886 Charleston, South Carolina, Earthquake." *Bulletin of the Seismological Society of America* **98**(5). p. 2533-2542.

Chapman, M.C., P. Talwani and R.C. Cannon (2003) “Ground motion attenuation in the Atlantic Coastal Plain near Charleston, South Carolina.” *Bulletin of the Seismological Society of America*. **93**. p. 998-1011

Chapman, M.C., E.C. Mathena and J.A. Snoke (2006). Southeastern United Sates Seismic Network Bulletin, no. 40, 36 pp. URL http://www.magma.geos.vt.edu/vtso/anonftp/catalog/, last accessed 12/15/2014.

Dewey, J. W. (1983). “Relocation of instrumentally recorded pre-1974 earthquakes in the South Carolina region.” Studies Related to the Charleston, South Carolina, Earthquake of 1886 Tectonics and Seismicity. G. S. Gohn, United States Geological Survey. p. Q1-Q9.

Dura-Gomez, I. (2004). “Seismotectonic framework of the Middleton Place Summerville Seismic Zone near Charleston, South Carolina.” Department of Geological Sciences. Columbia, South Carolina, University of South Carolina. Master of Science. 194 pp.

Dura-Gomez, I. and Talwani, P. (2009). "Finding Faults in the Charleston Area, SouthCarolina: 1. Seismological Data." *Seismological Research Letters* vol. **80,** no. 5, p. 883-900.

Dutton, C.E. (1889). “The Charleston earthquake of August 31, 1886.” in Ninth Annual Report of the U.S. Geological Survey, p. 203-528.

Gangophadyay, A. and Talwani, P. (2005). "Fault intersections and intraplate seismicity inCharleston, South Carolina: Insights from a 2-D numerical model." *Current Science,* vol. 88, no. 10, p. 1609-1616.

Gohn, G.S. et al. (1983). “Geology of the lower Mesozoic(?) sedimentary rocks in Clubhouse Crossroads test hole #3, near Charleston, South Carolina.” *in* Studies Related to the Charleston, South Carolina, Earthquake of 1886

-Tectonics and Seismicity, G.S. Gohn, editor, United States Geological Survey Professional Paper 1313, pp. D1-D17.

Gohn, G. S. (1983). "Geology of the basement rocks near Charleston, South Carolina-Data from detrital rock fragments in lower Mesozoic(?) rocks in Clubhouse Crossroads test hole #3." *in* Studies Related to the Charleston, South Carolina, Earthquake of 1886 -Tectonics and Seismicity. G. S. Gohn, editor, United States Geological Survey Professional Paper 1313, p. E1-E22.

Goldstein, P., A. Snoke, (2005), "SAC Availability for the IRIS Community", Incorporated Institutions for Seismology Data Management Center Electronic Newsletter. http://www.iris.edu/dms/newsletter/vol7/no1/sac-availability-for-the-iris-community/

Hamilton, R. M. et al. (1983). "Land multichannel seismic-reflection evidence for tectonic features near Charleston, South Carolina." *in* Studies Related to the Charleston, South Carolina, Earthquake of 1886-Tectonics and Seismicity. G. S. Gohn, editor, United States Geological Survey Professional Paper 1313, pp. I1-I18.

Johnston, A. C. (1995). "Seismic moment assessment of earthquakes in stable continental regions-111. New Madrid 1811-1812, Charleston 1886 and Lisbon 1755." *Geophys. J. Int.* 126, p. 314-344.

King, G.C.P. et al. (1994). "Static stress changes and the triggering of earthquakes." *Bulletin of the Seismological Society of America*, 84, p. 935-953.

Lahr, J. C. (1999). HYPOELLIPSE: A Computer Program for Determining Local Earthquake Hypocentral Parameters, Magnitude, and First-Motion Pattern. Open-File Report. 119 pp.

Lay, T., & Wallace, T. (1995). "Modern global seismology." Academic Press.

Lee, W. and Dodge, D. (2010). "Reliable Earthquake Location Using Grid-Search and Simplex Algorithm." Retrieved November 2014, from http://pubs.usgs.gov /of/2010/1152/presentations/of2010-1152_20100720g_lee.pdf.

Leutgert, J. H. et al. (1994). "Crustal Structure Beneath the Atlantic Coastal Plain of South Carolina." *Seismological Research Letters.* **65**(2). p. 180-191.

Long, L. T. and Champion, J.W. Jr. (1977). "Bouguer gravity map of the Summerville-Charleston, South Carolina, epicentral zone and tectonic implications." *in* Studies Related to the Charleston, South Carolina, Earthquake of 1886-A Preliminary Report, D. W. Rankin, editor, United States Geological Survey Professional Paper 1028, p.151-166.

Madabhushi, S. and Talwani, P. (1993). "Fault Plane Solutions and Relocations of Recent Earthquakes in Middleton Place Summerville Seismic Zone near Charleston, South Carolina." *Bulletin of the Seismological Society of America*, vol. 83, no. 5, p. 1442-1466.

Marple, R. T. and Talwani, P. (2000). "Evidence for a buried fault system in the Coastal Plain of the Carolinas and Virginia—Implications for neotectonics in the southeastern United States." *GSA Bulletin*, vol. 112, no. 2, p. 200-220.

McBride, J. H. et al. (1989). "Evidence and implications of an extensive early Mesozoic rift basin and basalt/diabase sequence beneath the southeast Coastal Plain." *GSA Bulletin*, vol. 101, p. 512-520.

McBride, J. H. (1991). "Constraints on the Structure and Tectonic Development of the Early Mesozoic South Georgia Rift, Southeastern United States; Seismic Reflection Data Processing and Interpretation." *Tectonics*, vol. 10, no. 5, p. 1065-1083.

Rankin, D. W. (1977). “Studies Related to the Charleston, South Carolina, Earthquake of 1886-Introduction and Discussion.” *in* Studies Related to the Charleston, South Carolina, Earthquake of 1886-A Preliminary Report. D. W. Rankin, editor, United States Geological Survey Professional Paper 1028, p. 1-16.

Snoke, J. A. (2003). "FOCMEC: FOCal MEChanism Determinations." Retrieved August, 2014, from http://www.geol.vt.edu/outreach/vtso/focmec/.

Taber, S. (1915). "Earthquakes in South Carolina During 1914." *Bulletin of the Seismological Society of America*, vol. 5, p. 96-99.

Taber, S. (1914). “Seismic activity in the Atlantic Coastal Plain near Charleston, South Carolina.” *Bulletin of the Seismological Society of America*, 4**,** p. 108-160.

Talwani, P. (2000). University of South Carolina. unpublished report.

Talwani, P. and Schaeffer, W.T. (2001). "Recurrence rates of large earthquakes in the South Carolina Coastal Plain based on paleoliquefaction data." *Journal of Geophysical Research*, vol. 106(B4). p. 6621-6642.

Tarr, A. C. (1977). “Recent seismicity near Charleston, South Carolina, and its relationship to the August 31, 1886, earthquake.” *in* Studies Related to the Charleston, South Carolina, Earthquake of 1886-A Preliminary Report. D. W. Rankin, editor, United States Geological Survey Professional Paper 1028, p. 43-58.

Tarr, A. C. and Rhea, S. (1983). “Seismicity near Charleston, South Carolina, March 1973 to December 1979.” *in* Studies Related to the Charleston, South Carolina, Earthquake of 1886-Tectonics and Seismicity, G. S. Gohn, editor, United States Geological Survey Professional Paper 1313, p. R1-R17.

Tarr, A. C. et al. (1981). "Results of Recent South Carolina Seismological Studies." *Bulletin of the Seismological Society of America,* 71, p. 1883-1902.

Waldhauser, F. (2001). hypoDD-A Program to Compute Double-Difference Hypocenter Locations, United States Geological Survey Open-File Report 2001-113, 25 p. URL http://pubs.er.usgs.gov/publication/ofr01113, accessed 12/14/2014.

Waldhauser, F. and W. L. Ellsworth (2000). "A Double-Difference Earthquake Location Algorithm: Method and Application to the Northern Hayward Fault, California." *Bulletin of the Seismological Society of America*, 90, p. 1353-1368.

Wong et al. (2005). "Potential Losses in a Repeat of the 1886 Charleston, South Carolina, Earthquake." *Earthquake Spectra,* vol. 21, no. 4, p. 1157-1184.

Wu, Q. et al. (2015). "Investigation of the aftershock sequence of the August 23, 2011 Mineral, Virginia, Earthquake." *Seismological Research Letters*, in press 2015.

Yantis, B. R. and Costain, J.K. (1983). "A reflection seismic study near Charleston, South Carolina." *in* Studies Related to the Charleston, South Carolina, Earthquake of 1886 Tectonics and Seismicity. G. S. Gohn, editor, United States Geological Survey Professional Paper 1313, p. G1-G20.

Zoback, M. L., 1992. "Stress field constraints on intraplate seismicity in Eastern North America." *Journal Geophysical Research***,** 97, p. 11761-11782.

Appendix A: Figures
Chapter 1:

Intensity	Magnitude	Shaking/Damage
I	1.0-3.0	Not felt in most cases.
II	3.0-3.9	Weak shaking; Felt by only a few, especially those on upper floors of buildings
III	3.0-3.9	Weak shaking; Felt by people indoors; Duration can be estimated.
IV	4.0-4.9	Light shaking; Felt by people indoors and outdoors; Dishes, windows, doors disturbed.
V	4.0-4.9	Moderate shaking; Felt by most people; Windows, dishes broken.
VI	5.0-5.9	Strong shaking; Felt by all; Minor damage, heavy furniture moved, fallen plaster.
VII	5.0-5.9	Very strong shaking; Slight-moderate damage of well-built structures; considerable damage to to poorly built structures; broken chimneys.
VIII	6.0-6.9 or > 7.0	Severe shaking; Partial collapse of substantial structures; fall of chimneys, factory stacks, columns, monuments, walls.
IX	6.0-6.9 or > 7.0	Violent shaking; Damage great in most structures;Buildings shifted off foundations.
X	> 7.0	Extreme shaking; Some well-built wooden structures destroyed; Most masonry and frame structures destroyed; Railroads bent.
XI	> 7.0	Extreme shaking; Few structures lefft standing; Bridges destroyed; Railroads extremely bent.
XII	> 7.0	Damage total; Objects thrown into air.

Adapted from the United States Geological Survey, Earthquake Hazards Program
Earthquake Topics for Education webpages:
earthquake.usgs.gov/learn/topics/mag_vs_int.php
earthquake.usgs.gov/learn/topics/mercalli.php

Figure 1.1: A diagram showing the Modified Mercalli Intensity (MMI) Scale. The intensity ranges from Roman Numerals I-XII, where I is the weakest and XII is the most severe. These intensities are assigned based on shaking and structural damage reports. Each intensity is associated with a range of earthquake magnitude.

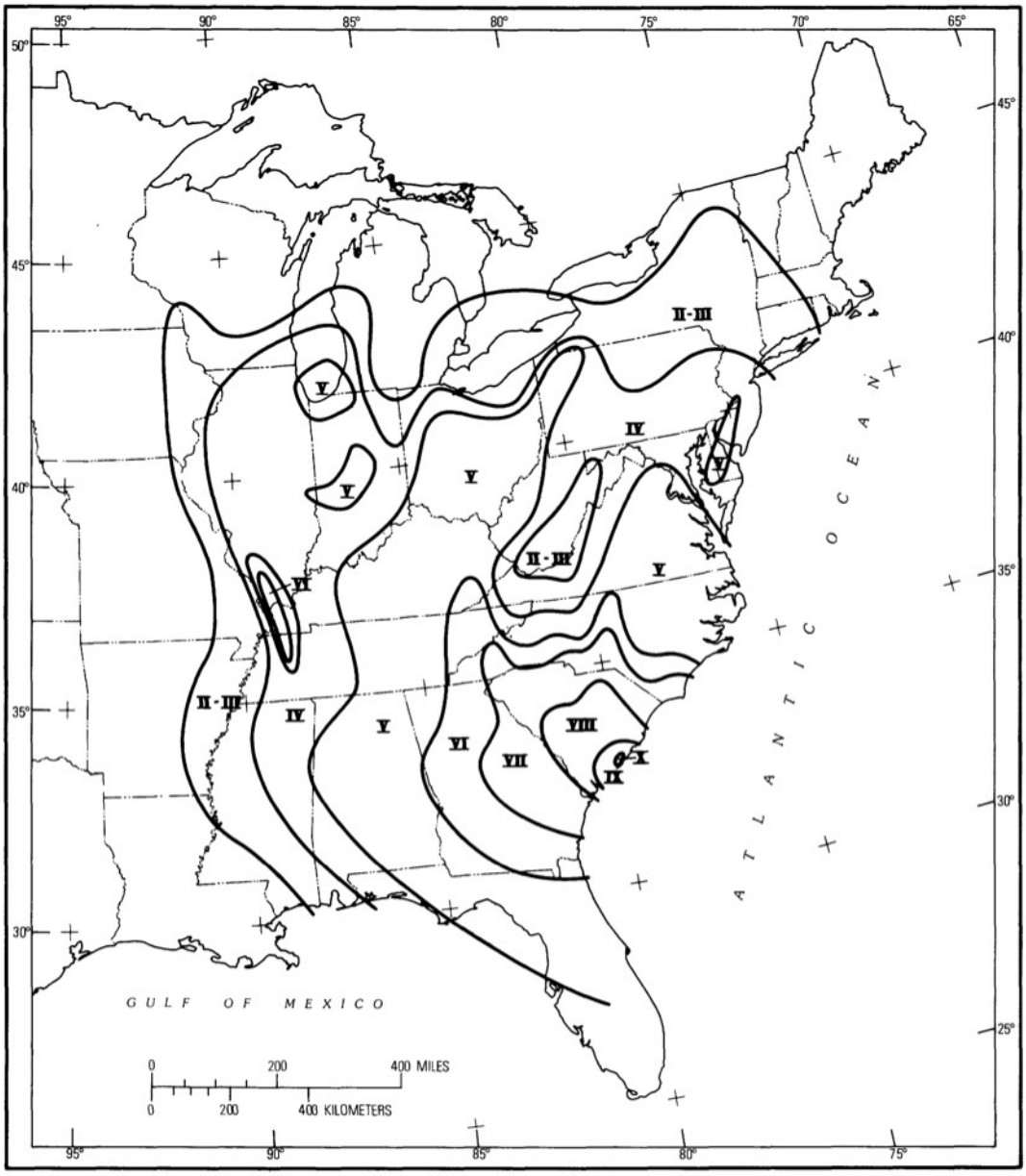

Figure 1.2: A contoured MMI map for the 1886 Charleston earthquake. The epicentral region had an intensity of X, and areas as far North as Canada and as far South as Cuba had reported intensities of II-III. Reference: Bollinger, G. A. (1977), used with permission (public domain, report does not specify copyrights; URL: http://www.usgs.gov/visual-id/credit_usgs.html).

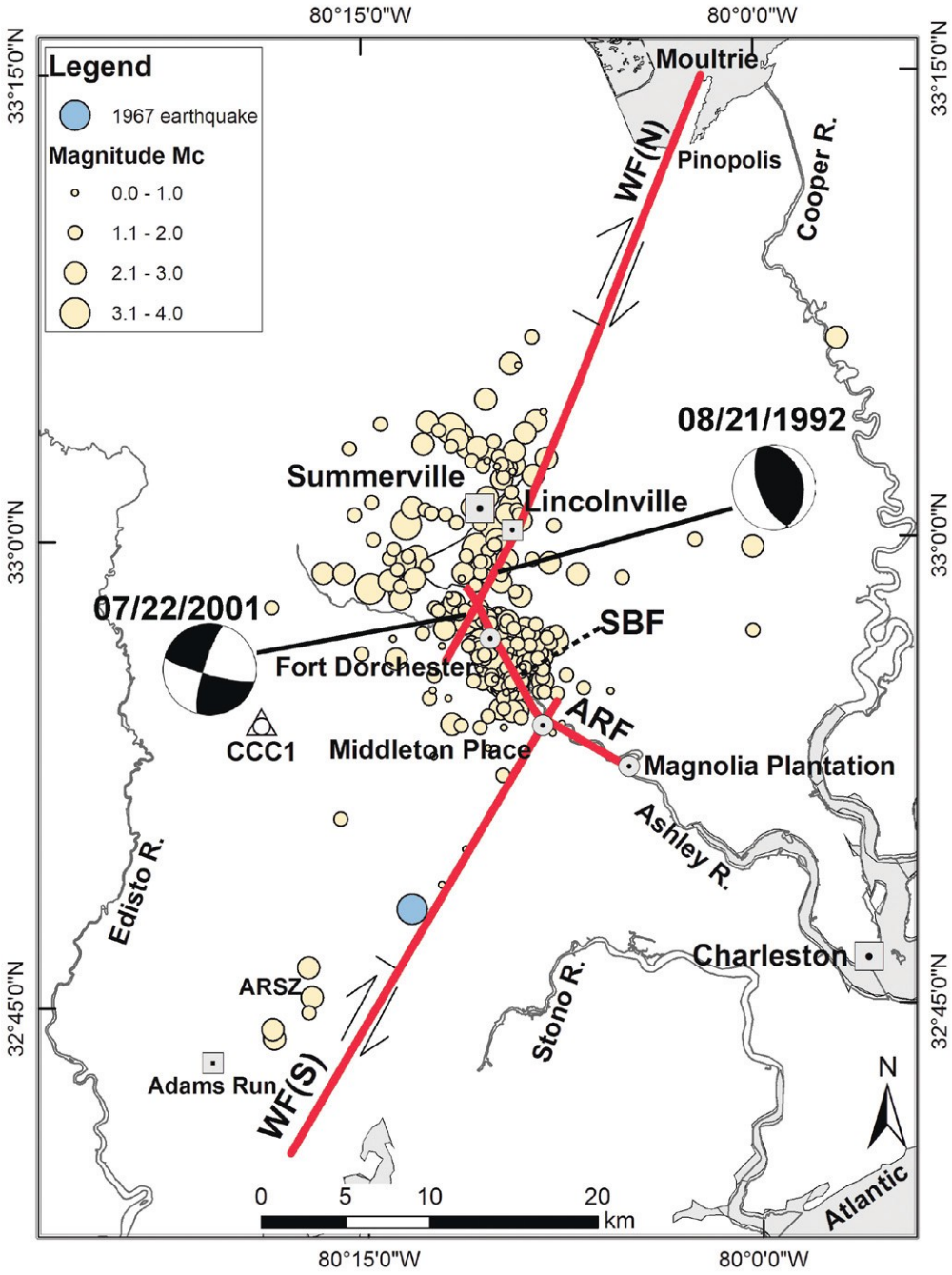

Figure 1.3: A proposed fault model for the study region. It contains an approximately 50 kilometer long NE-SW trending fault, called the Woodstock Fault (WF) with a step over fault trending to the NW-SE called the Sawmill Branch fault (SBF). Additionally there is a fault, branching off to the East called the Ashley River Fault (ARF). The circles represent located events between 1974-2004 from the South Eastern United States Seismic Network (SEUSSN). Reference: Dura-Gomez, I. and Talwani, P. (2009), used with permission from SSA (http://www.seismosoc.org/publications/permissions.php).

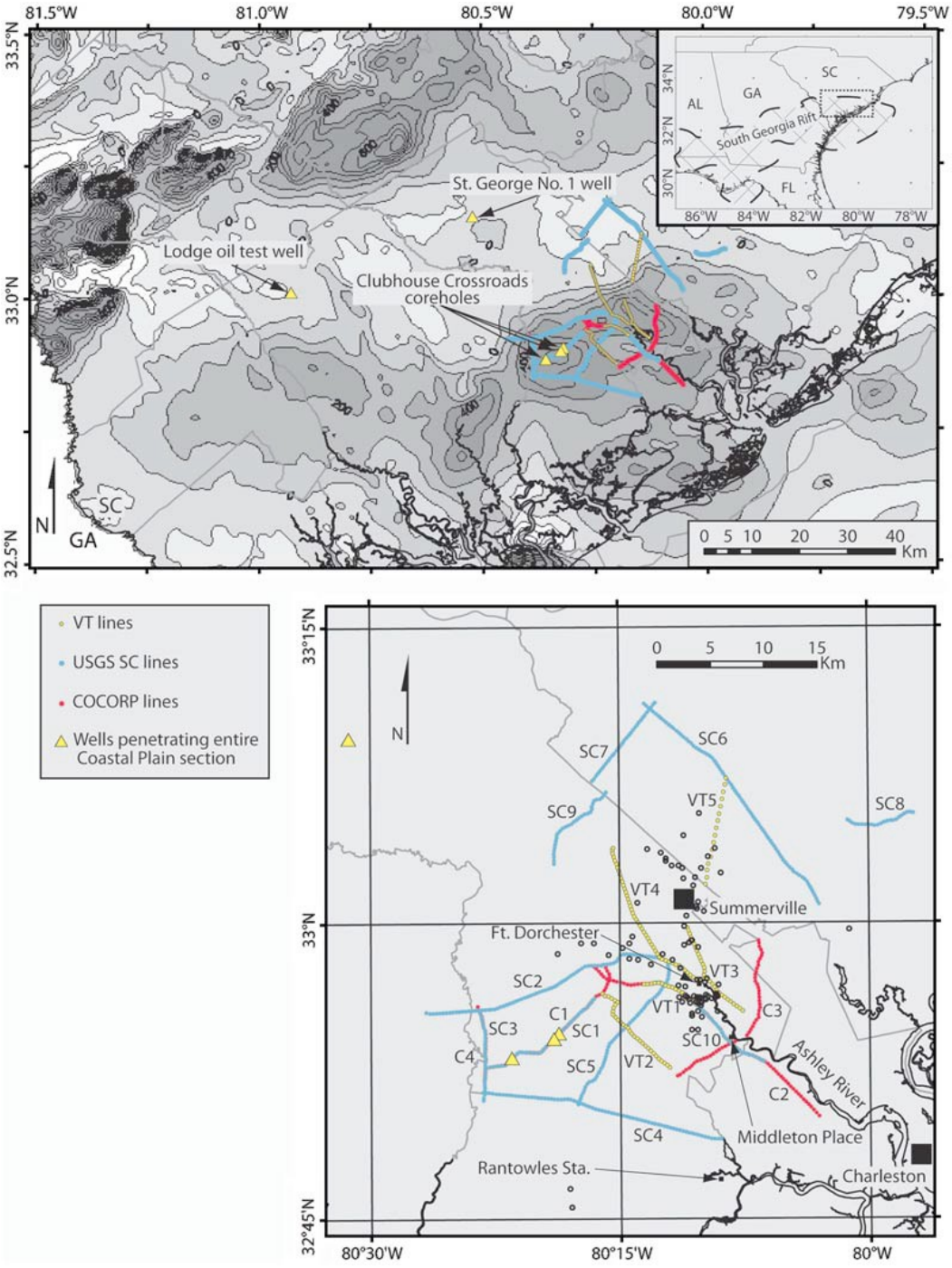

Figure 1.4: Detailed maps of the study region. Top: A magnetic intensity map of the study region. The colored lines represent the seismic reflection profiles from VT, USGS, and COCORP, and the wells are marked by the yellow triangles. The study region lies on a magnetic anomaly. Bottom: A more-detailed map of the study area, showing the rivers and county lines. The circles represent earthquakes epicenters (M > 2) from 1977-2004, located by the SEUSSN. Reference: Chapman, M. C. and Beale, J.N. (2010), used with permission from M.C. Chapman.

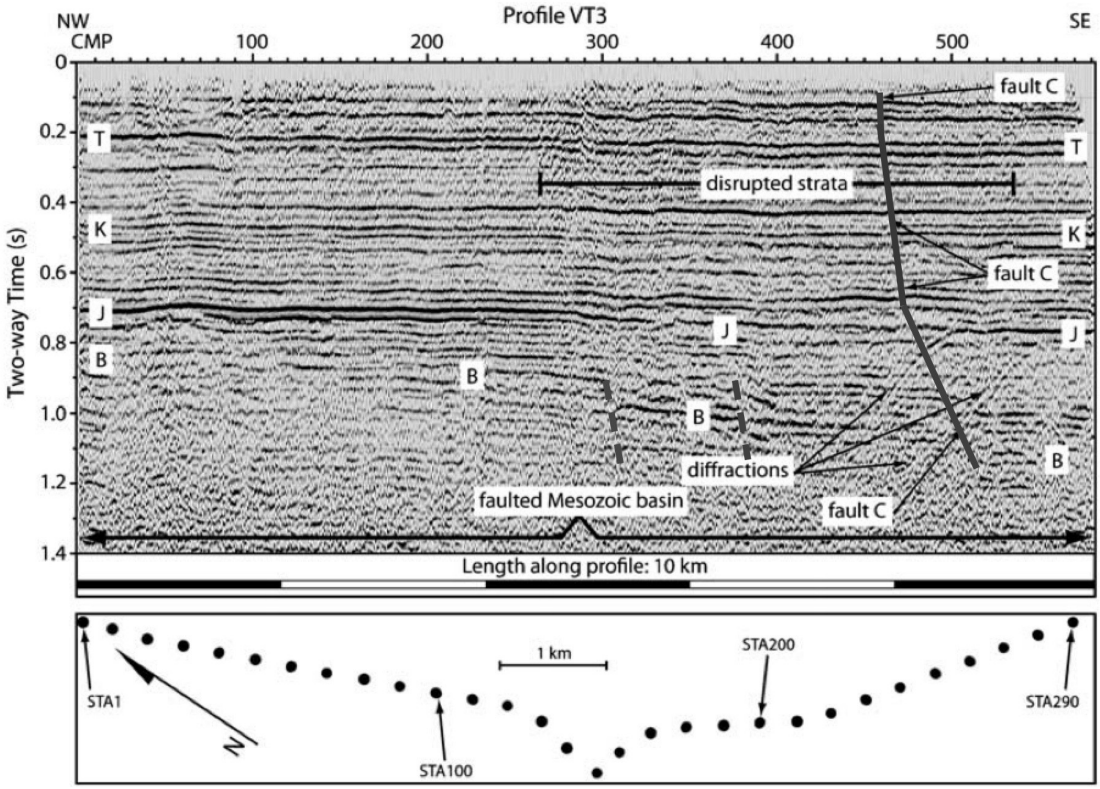

Figure 1.5: Processed seismic reflection profile VT3. Interpreted faults and reflectors are annotated. The bottom of the figure shows the reflection profile in map view. Reference: Chapman, M. C. and Beale, J.N. (2010), used with permission from M.C. Chapman.

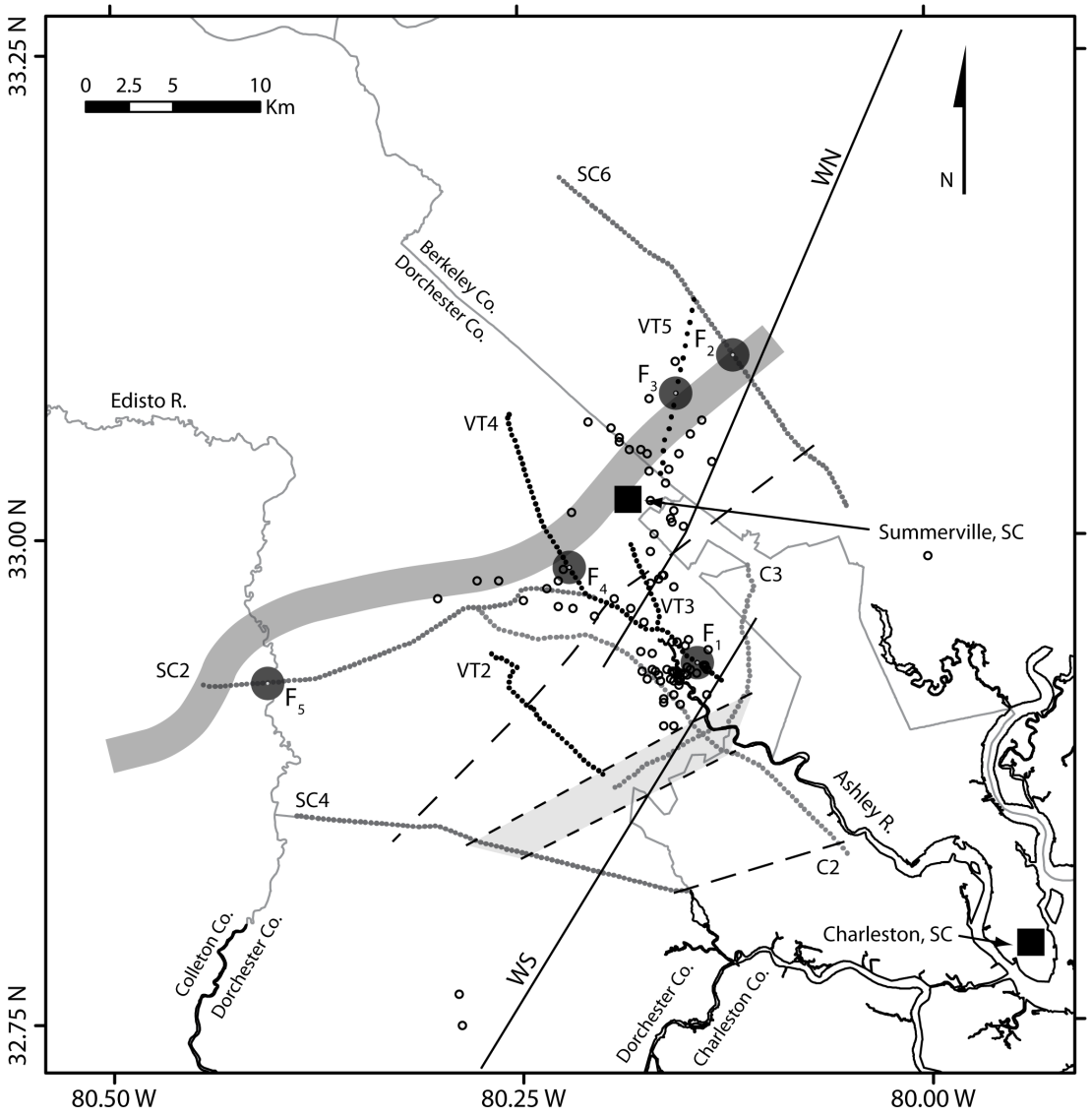

Figure 1.6: A map of the study region showing the magnetic gradient and imaged faults. The lines composed of small dots show the locations of seismic reflection profiles (each dot is a profile station location). The location of the gradient in the magnetic field is indicated by the broad shaded line. The locations of Mesozoic-Cenozoic faults imaged on reflection profiles are indicated by the large filled circles, labeled F1 through F5. Small open circles show earthquake epicenters (M>2.0, occurring from 1977 through 2004) located by the University of South Carolina seismic network. The long-dashed line passing approximately 4 km southeast of Summerville marks the location where southeastward dip on the bright B reflection becomes pronounced. The long-dashed line near the end of profiles C2 and SC4 marks the location where the bright B reflection shallows to the level of the J reflection, dipping to the northwest. The trough of the intervening structural basin, defined by two-way time greater than 1.1 second for the bright B reflection, is indicated by the shaded area outlined by short-dashed lines containing the southern part of reflection profile C3. The inferred Woodstock North (WN) and Woodstock South (WS) faults of Dura-Gomez and Talwani (2009) are shown as solid lines. From Chapman and Beale (2010), used with permission from M.C. Chapman.

Chapter 2:

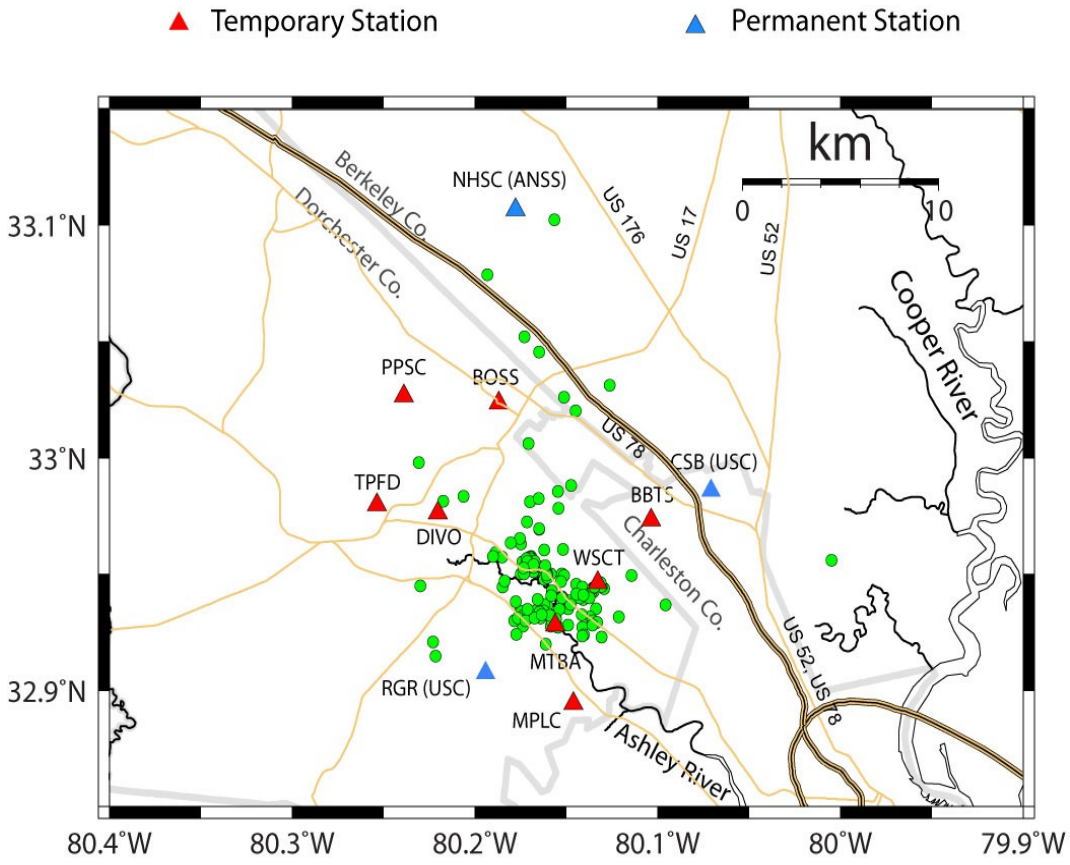

Figure 2.1: The seismic network used for the monitoring experiment: The red triangles represent the eight temporary stations and the blue triangles represent the 4 permanent stations, sponsored by the ANSS (USGS) and run by the University of South Carolina. The black dots represent 134 earthquakes located by HypoEllipse (duration magnitudes ranging from -1.8-2.6).

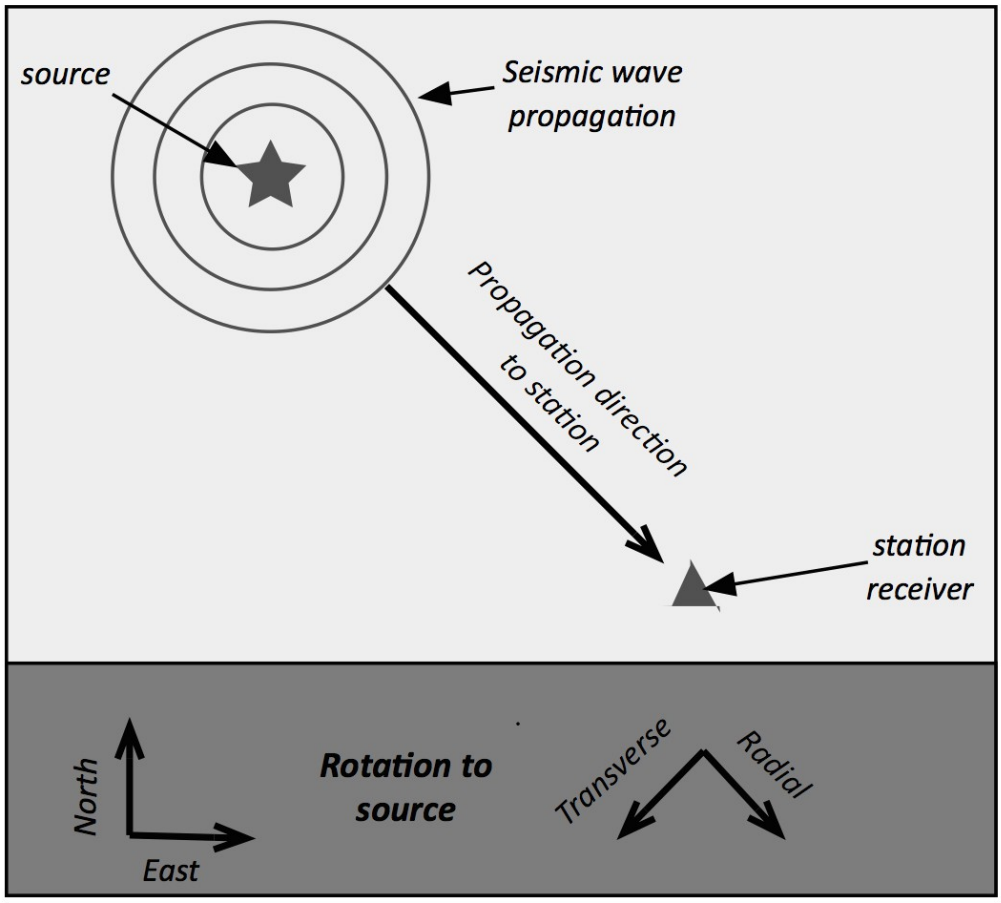

Figure 2.2: A diagram illustrating the rotation of horizontal station components. . The rotation, described by Equation 2, transforms the North and East components to the Radial and Transverse components, respectively and effectively rotates the components to the direction of source propagation.

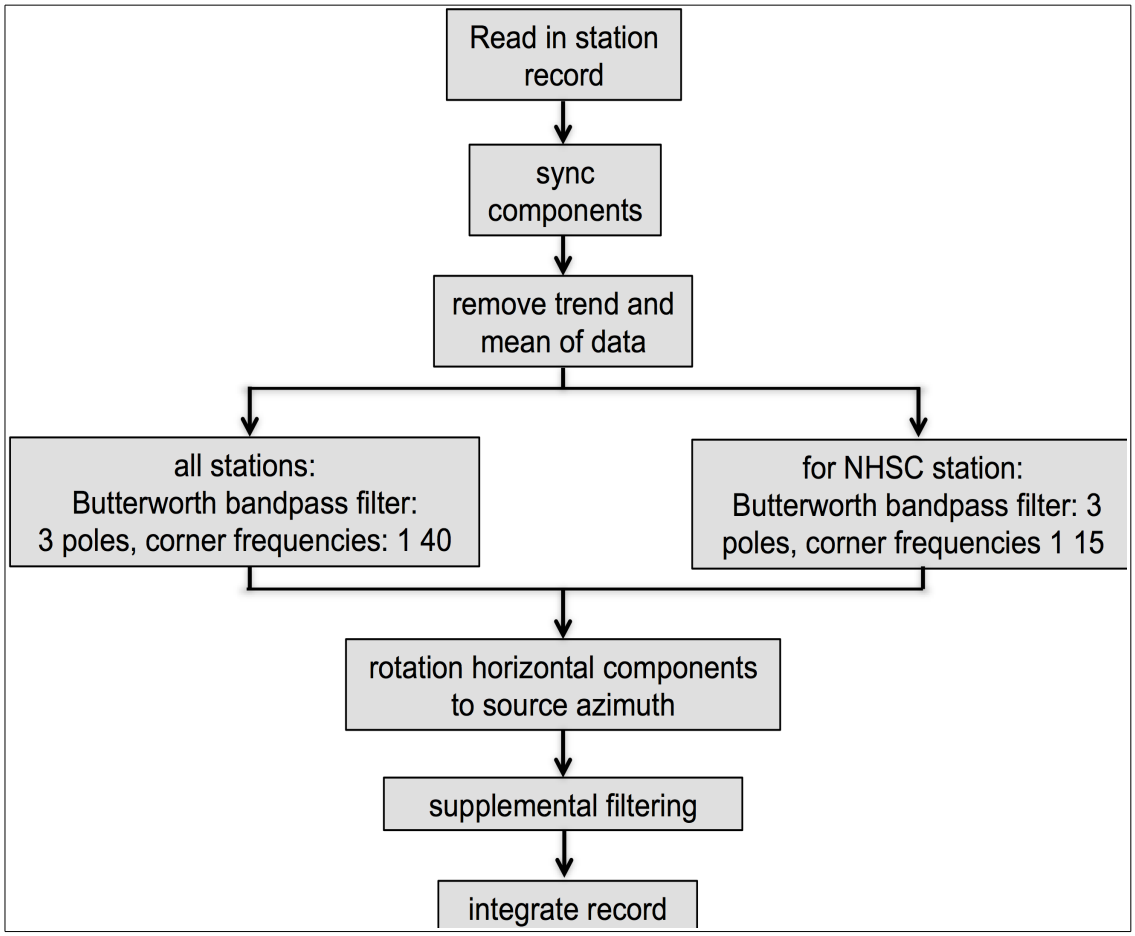

Figure 2.3: A flow chart outlining the processing steps carried out for each station record. The Butterworth bandpass filters were chosen, to reduce low-frequency noise and high-frequency acausal energy from the instrument FIR filter. The source azimuth was determined by initial location of the 134 detectable events from Hypoellipse. The supplemental filtering was an iterative process and the filters were chosen based on comparison of the Fourier amplitude spectra of the signal and pre-signal noise.

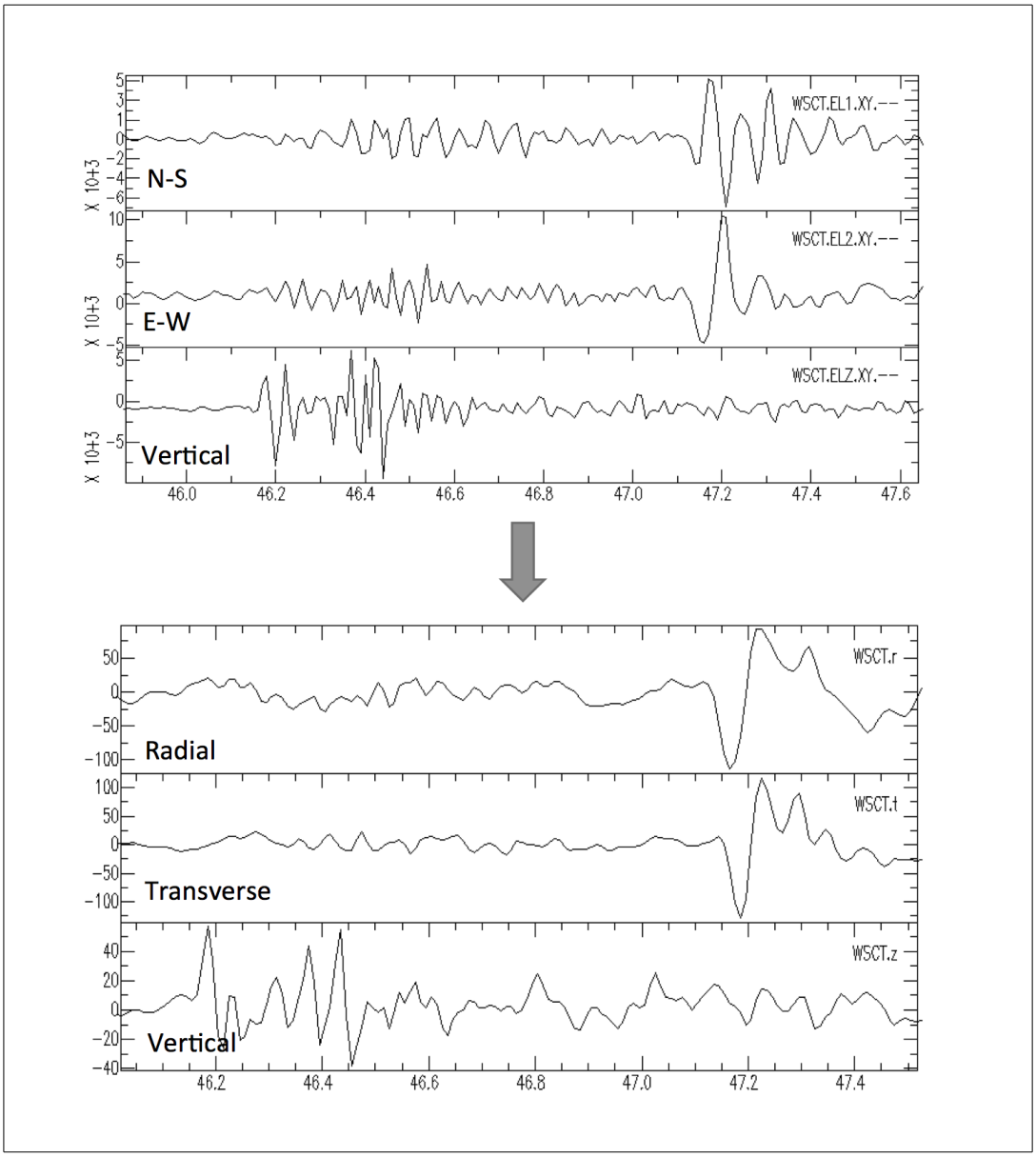

Figure 2.4: A diagram comparing raw data and processed data. Top: Unprocessed 3-component station record (WSCT): North-South, East-West, and Vertical components. Bottom: Processed record (see flow chart in Figure 2.3): Radial, Transverse, Vertical components.

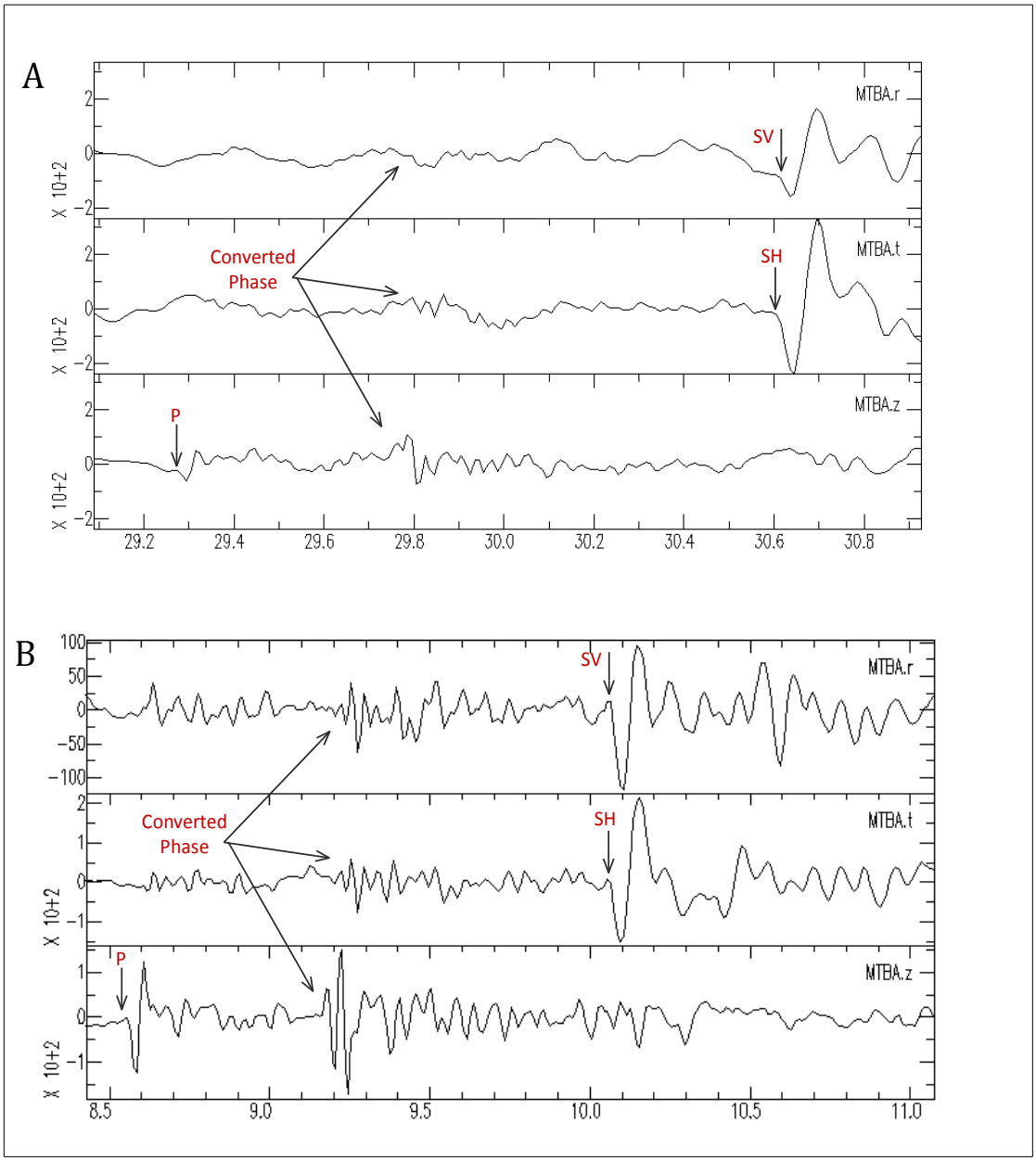

Figure 2.5: A: Processed 3-component station record (MTBA) with interpreted wave phases. The P wave is picked on the vertical component, the SH wave is picked on the transverse component, and the SV wave is picked on the radial component. The converted phase is also annotated, and in some cases is hard to distinguish with the S wave, particularly the SV wave. B: Another example of a processed record (MTBA) with interpreted wave phases and a large converted phase.

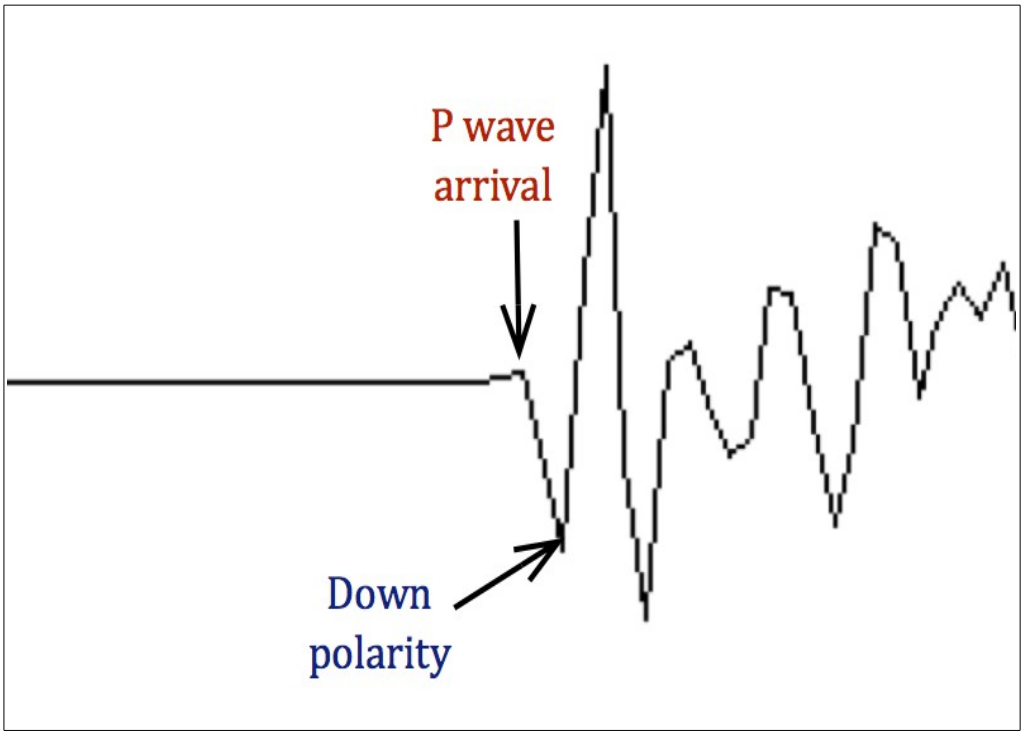

Figure 2.6: A diagram showing the convention of picking a wave phase. The polarity is determined by the peak or trough at the next half cycle following the arrival time. Polarity conventions for all wave phases are summarized in Table 2.

Chapter 3:

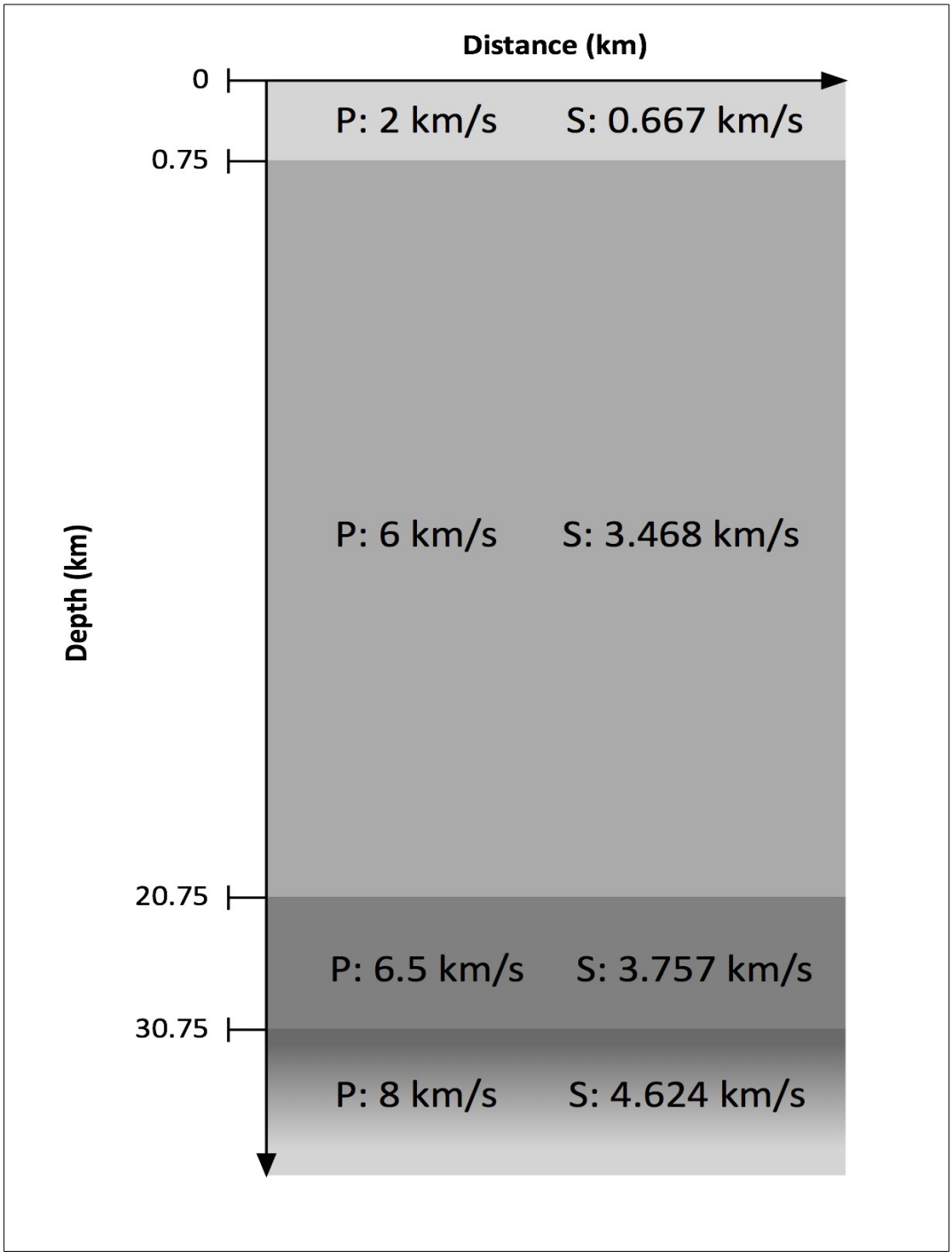

Figure 3.1: A diagram showing the 1-D velocity model. It is 3 layers over a halfspace, derived from Chapman et al. (2003). It incorporates a shallow layer with low P and S wave velocities appropriate for the coastal plain sediments, a higher velocity, upper crustal layer representative of the lower Mesozoic volcanic and sedimentary rock section, and a lower crustal velocity layer with somewhat higher wave velocities determined from refraction velocity measurements in the Piedmont province of Virginia (Bollinger et al., 1980).

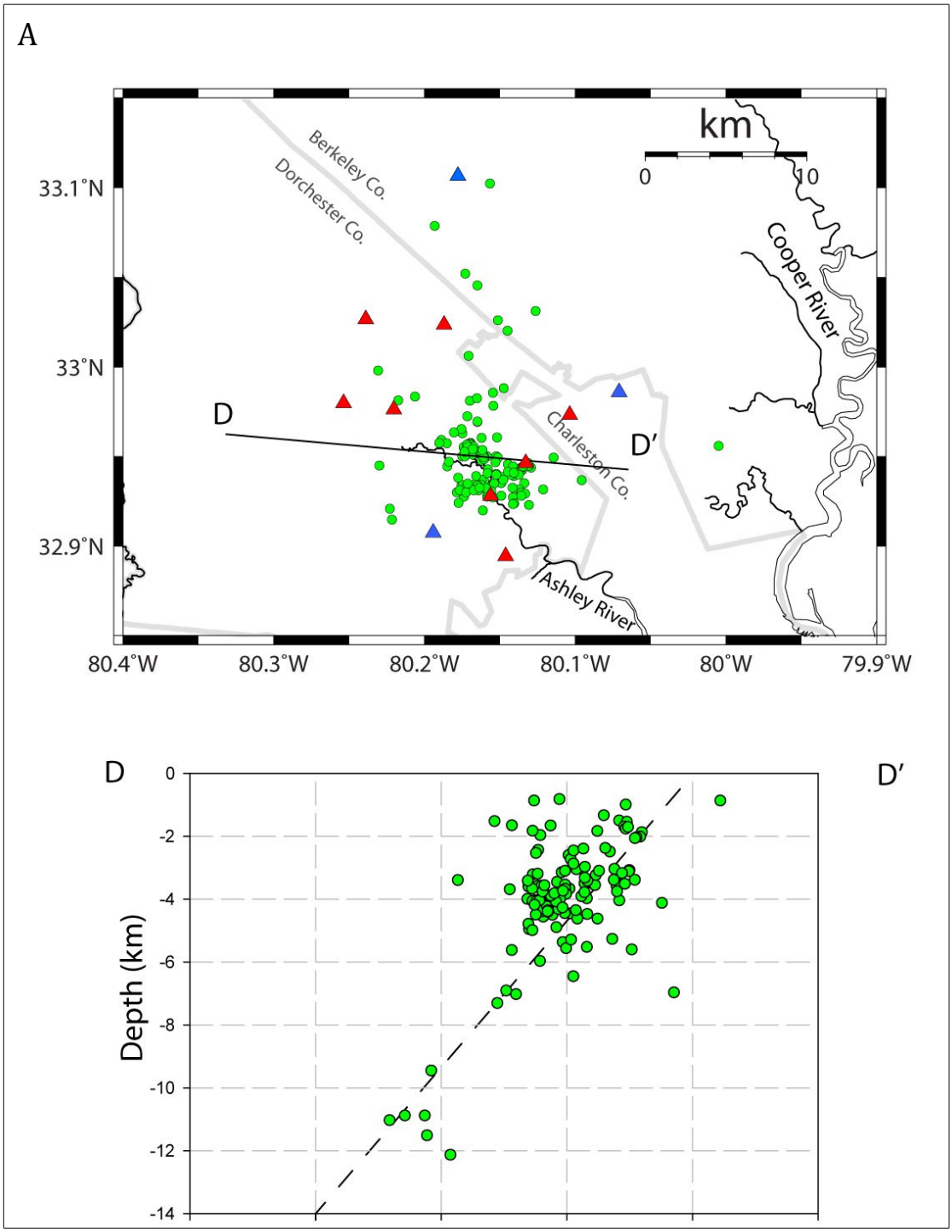

Figure 3.2A: Hypocenter locations with Hypoellipse. Top: Hypocenter locations of 134 earthquakes determined using Hypoellipse, plotted as epicenters in map view. A cross-section D-D' trending N95E is projected through the earthquakes. Bottom: The D-D' cross section is shown, illuminating a possible trend (dashed line) of the hypocenters. Most of the events are within the upper 5 km.

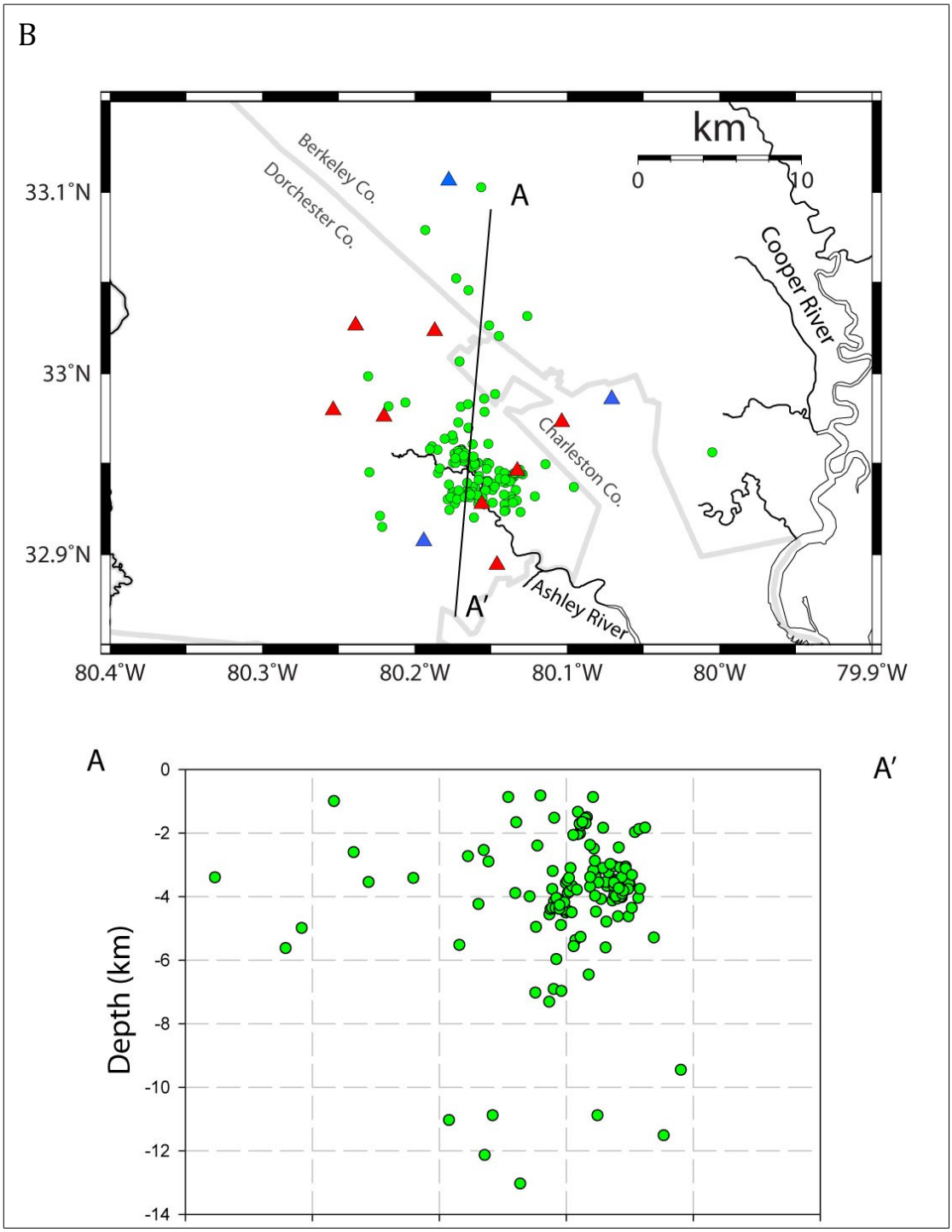

Figure 3.2B: Hypocenter locations with Hypoellipse: a different perspective. Top: Hypocenter locations of 134 earthquakes determined using Hypoellipse, plotted as epicenters in map view. A cross-section A-A trending N5E is projected through the earthquakes. Bottom: The A-A' cross section is shown and are within the upper 5 km.

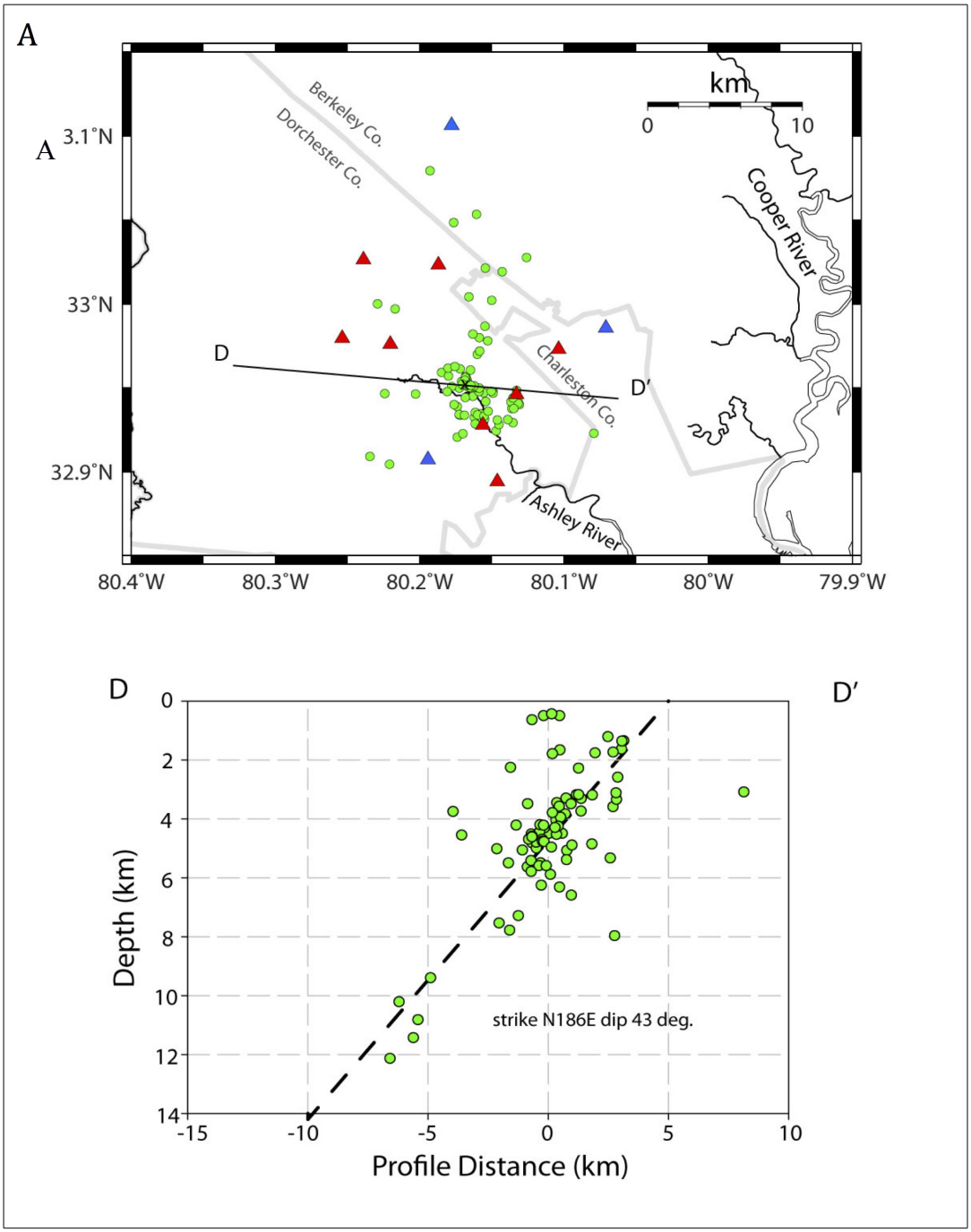

Figure 3.3A: Hypocenter locations with HypoDD. Top: Hypocenter re-locations of 87 earthquakes determined using HypoDD, plotted as epicenters in map view. A cross-section D-D' trending N95E is projected through the earthquakes. Bottom: The D-D' cross section is shown, illuminating a trend(dashed line) of the hypocenters, which is more clearly defined in the re-locations. A least squaresplane fitted to the hypocenters is shown as the dashed line, with strike N186E and dip 43 degrees to the West.

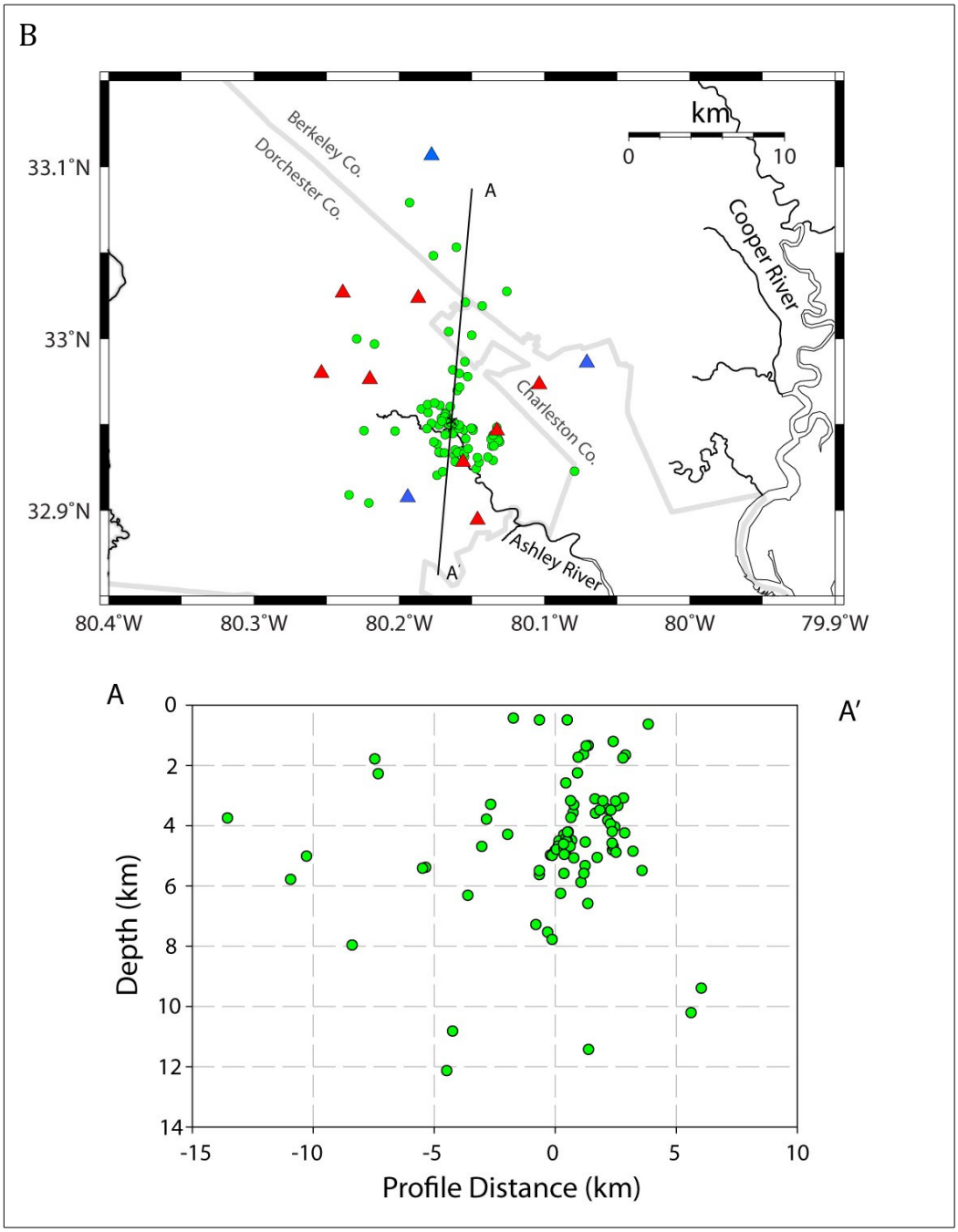

Figure 3.3B: Hypocenter locations with HypoDD: a different perspective. Top: Hypocenter re-locations of 87 earthquakes determined using HypoDD, plotted as epicenters in map view. A cross-section A-A' trending N5E is projected through the earthquakes. Bottom: The A-A' cross section is shown, and the hypocenters appear scattered with two localized clusters between 0 and 5 km in profile distance and at approximately 4 km depth.

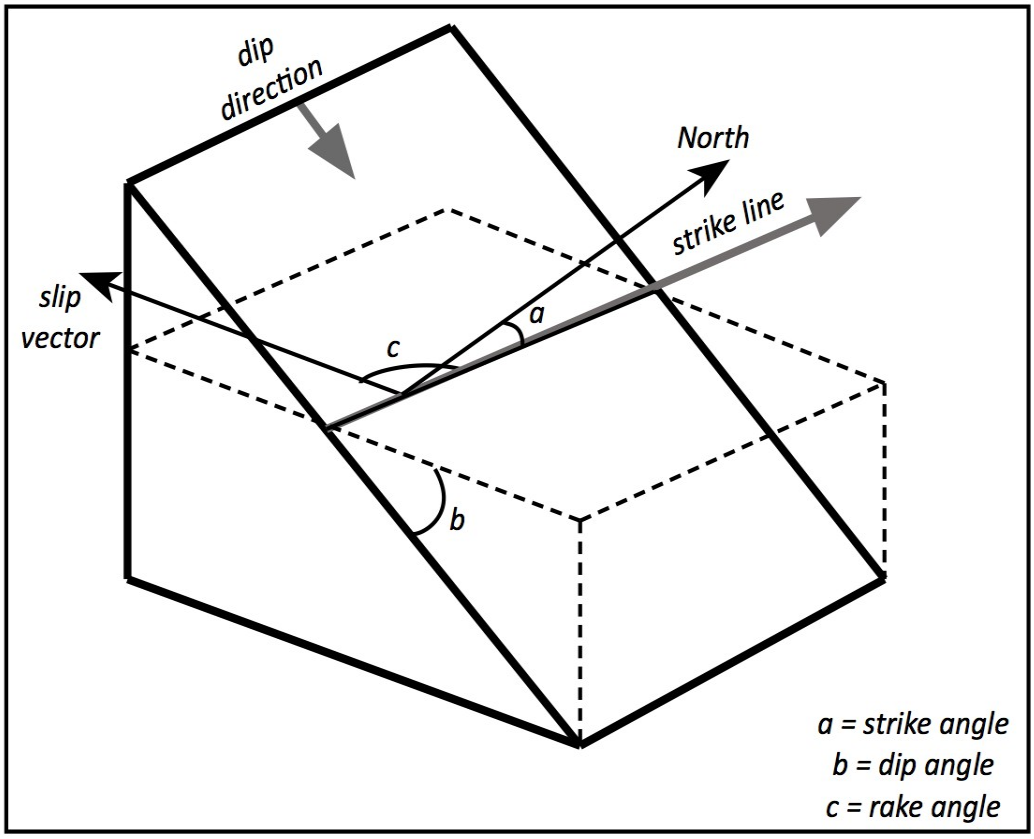

Figure 3.4: A diagram summarizing definitions of strike, dip, and rake. The strike line is defined as the intersection between the planar feature and a horizontal plane in space. The strike azimuth, a, is the angle between the strike line and geographical North. The dip direction is orthogonal to the strike line, measured clockwise. The dip direction, b, is the angle between the horizontal plane and the planar feature. The slip vector is defined as the direction and magnitude of displacement of the hanging wall with respect to the footwall and the rake angle, c, is the angle between the slip vector and the strike line, positive in the counter-clockwise direction.

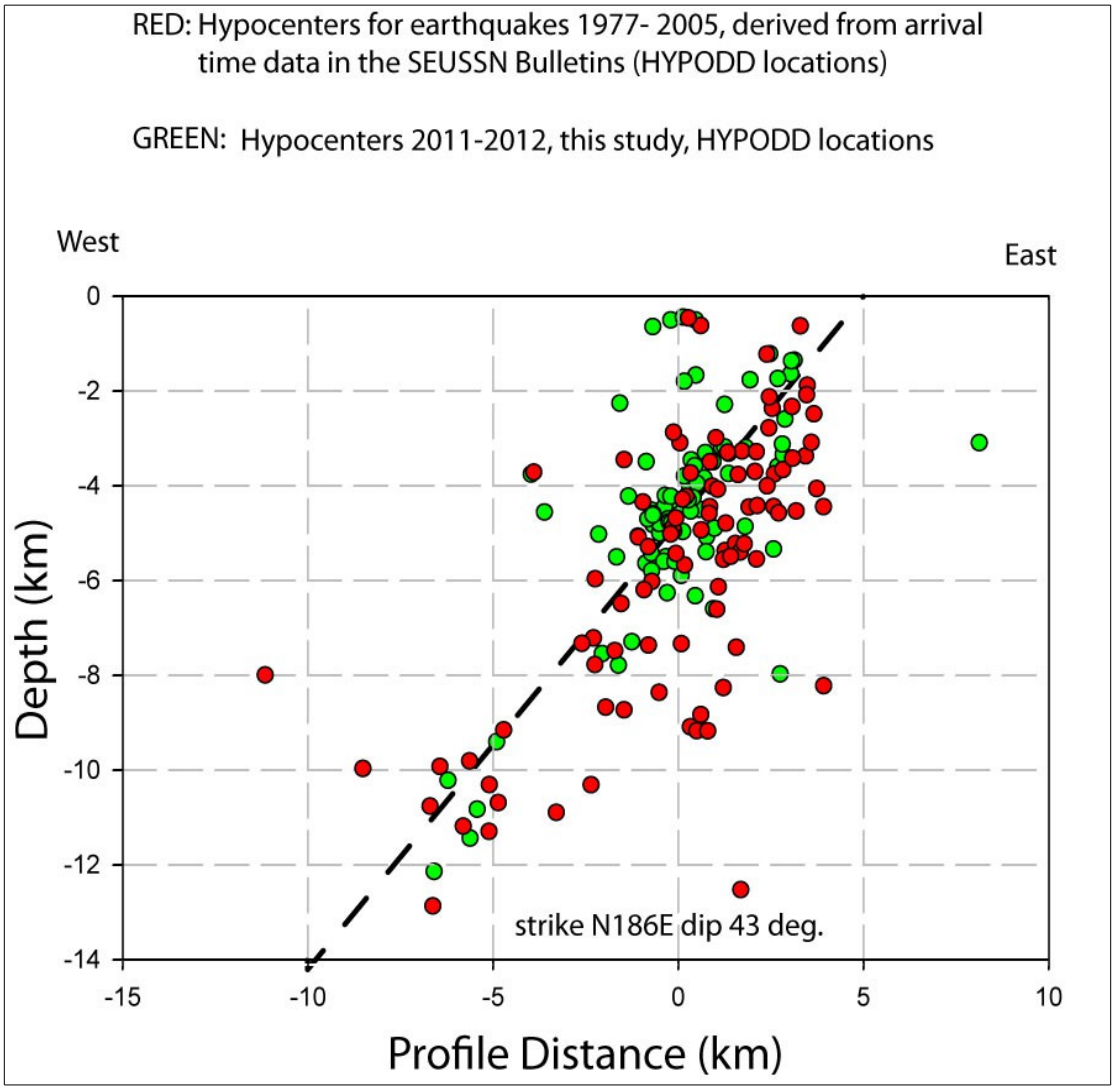

Figure 3.5: A comparison of hypocenter locations from two seismic networks. The green dots represent the hypocenters located in this study and the red represent hypocenters located from the SEUSSN (South East United States Seismic Network). The hypocenters were located by Jake Beale and Qimin Wu, using the same procedure as described in Chapter 3. The hypocenters from both networks are significantly consistent in terms of overall trend.

Chapter 4:

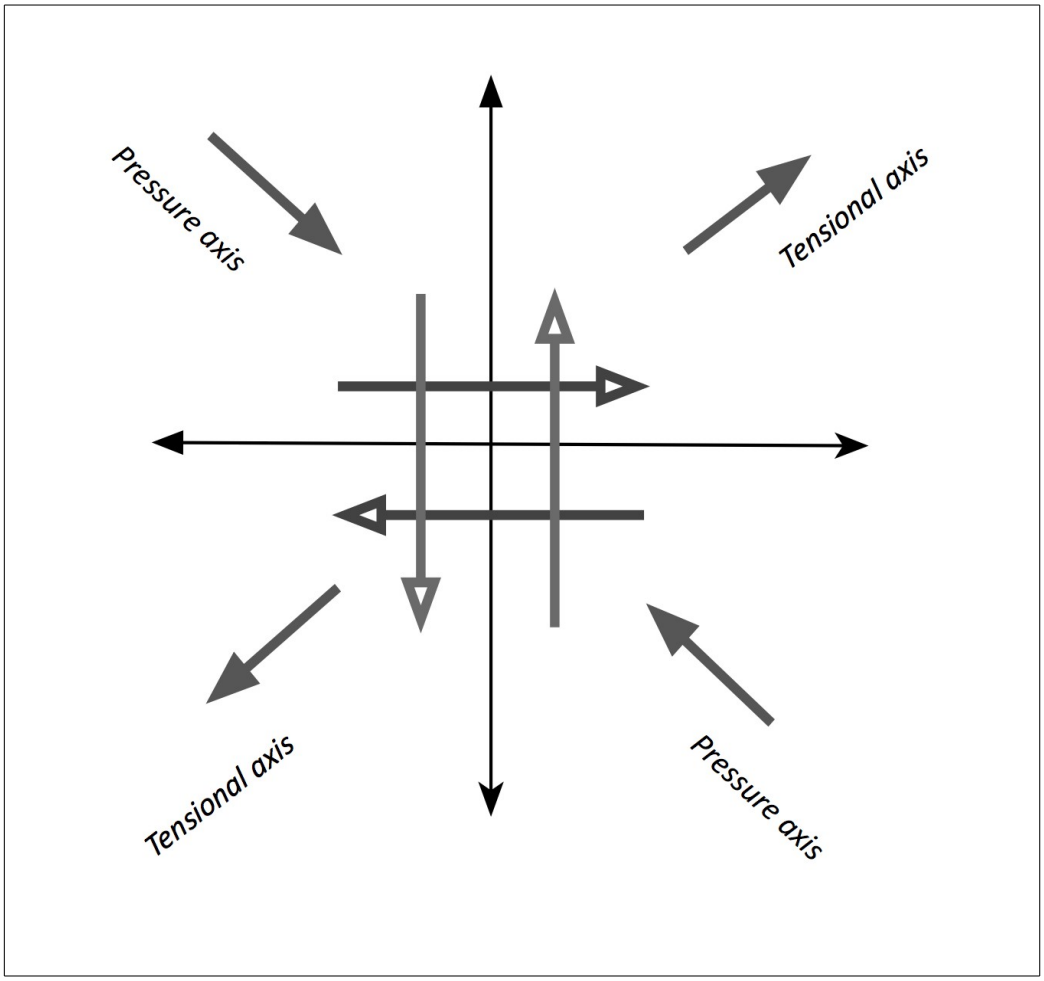

Figure 4.1: A diagram summarizing the double-couple force system. The double couple represents the force system (open arrows) responsible for shear dislocation on a plane, and is a subset of general seismic moment tensors, which characterize the motion of an earthquake source. It is assumed that moment tensors of all the events considered in this study are pure double couple.

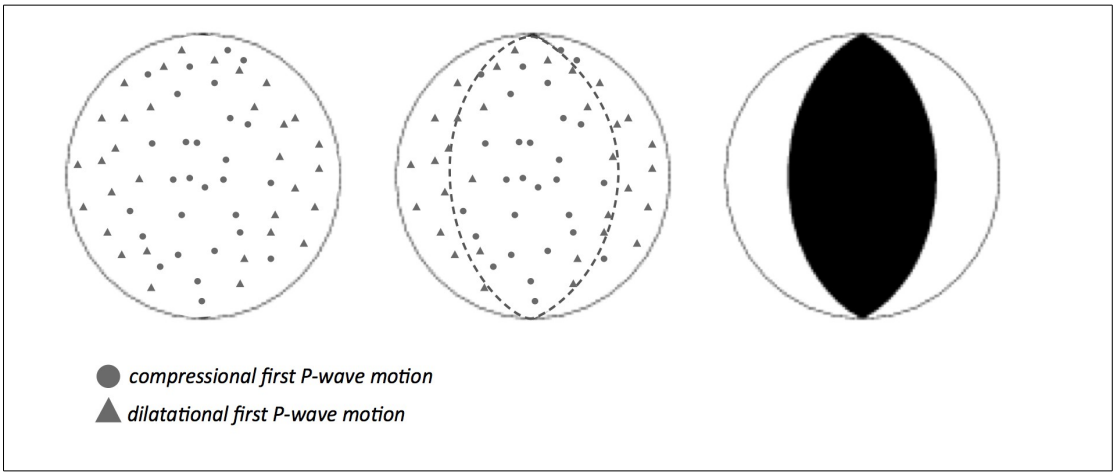

Figure 4.2: A diagram of determining focal mechanisms from P-wave first motions. Focal mechanisms can be derived from first motions polarities of wave phases (left). The circles represent P-wave compressional motion, or motion towards the source ('down' polarity on three-component record). The triangles represent P-wave dilatational motion, or motion away from the source ('up' polarity on three-component record). The focal sphere can be divided into quadrants based on compressional and dilatational first motions (middle). By convention the P-wave compressional motion quadrant is shaded in black to form a beachball diagram (right).

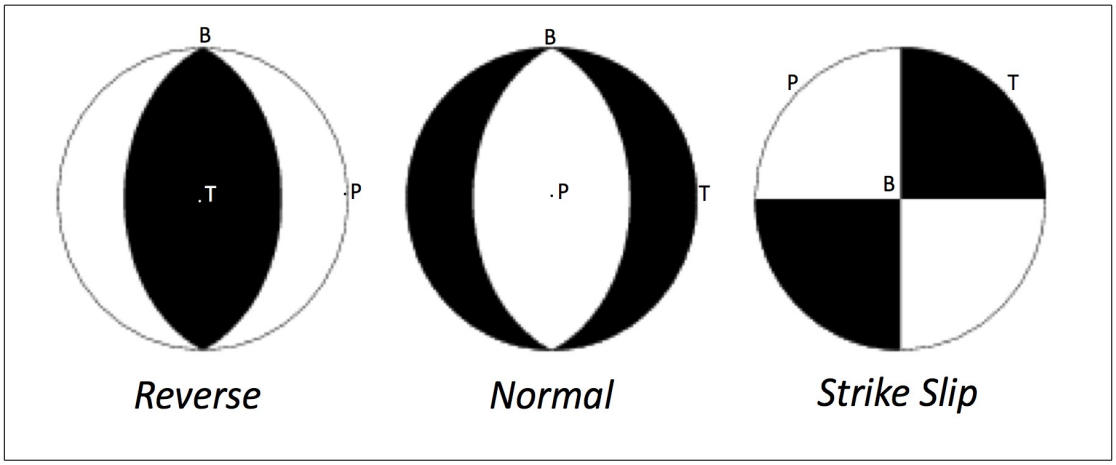

Figure 4.3: A diagram showing the beachball diagrams for the 3 fundamental fault types. They include dip slip with reverse motion, dip slip with normal motion, and strike slip. There are three axes plotted on a focal mechanism/beach ball diagram: Tensional (T), Compressional/Pressure (P), and the Null (B or N). The tensional axis is located at the center of the P-wave compressional quadrant, the pressure axis is located at the center of the P-wave dilatational quadrant, and the null axis marks the intersection of the two nodal planes.

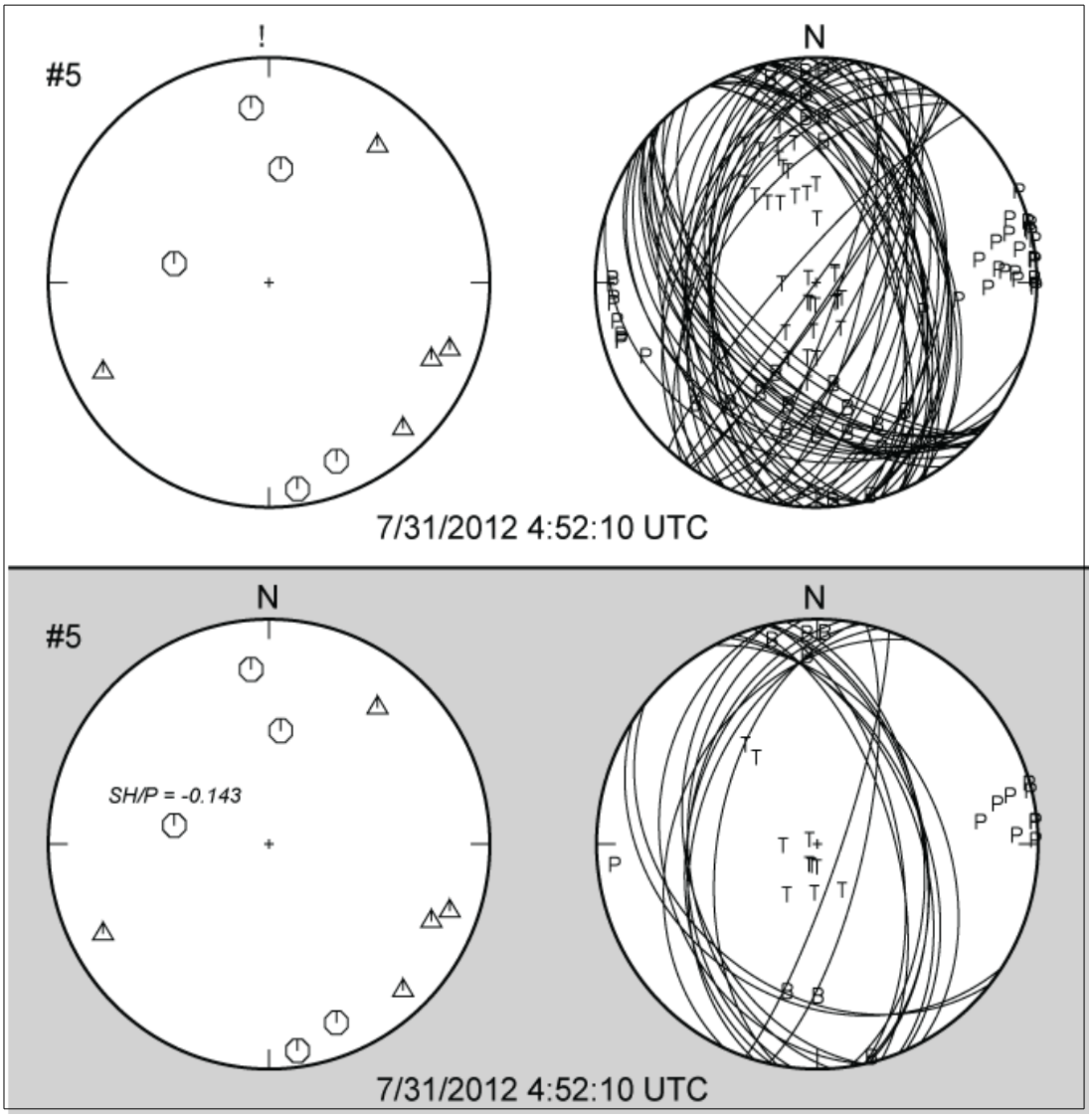

Figure 4.4: Comparison of focal mechanism solutions derived from different data types. Top: The focal mechanism solutions (Focmec output), derived from P-wave first motion polarity data. Bottom: The addition of a single amplitude ratio greatly improves the constraint of the focal mechanism solution by reducing the amount of possible fault-plane solutions. Reference: Chapman, M. C. and Beale, J.N. (2013), used with permission from M.C. Chapman.

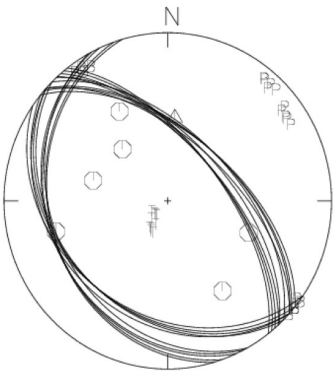

Event 20110807_043200 :
best solution

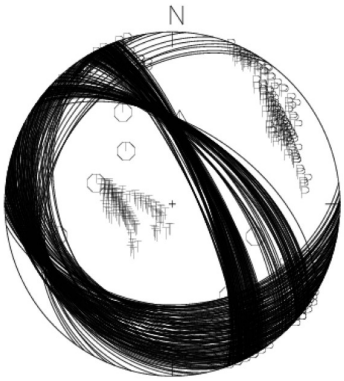

Event 20110807_043200 :
Initial Constraint Test
Addition of 1 polarity

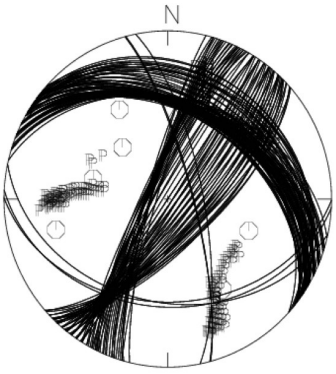

Event 20110807_043200 :
Ratio Constraint test

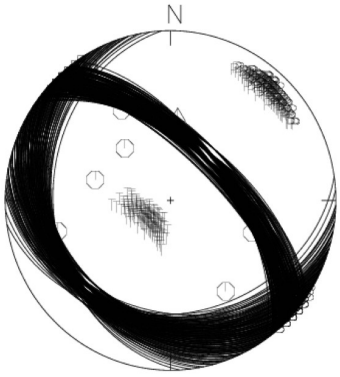

Event 20110807_043200 :
Polarity Constraint test

	Allowed Polarity errors	Allowed Ratio errors	# solutions
Top Left	0	3	10
Top Right	1	3	142
Bottom Left	500	0	148
Bottom Right	0	500	148

Figure 4.5: Focal mechanism solutions and constraint tests for an event in the dataset. Both the best solution (top left) and the outputs from the constraint tests are shown. Constraint testing reveals how robust the best solution is.

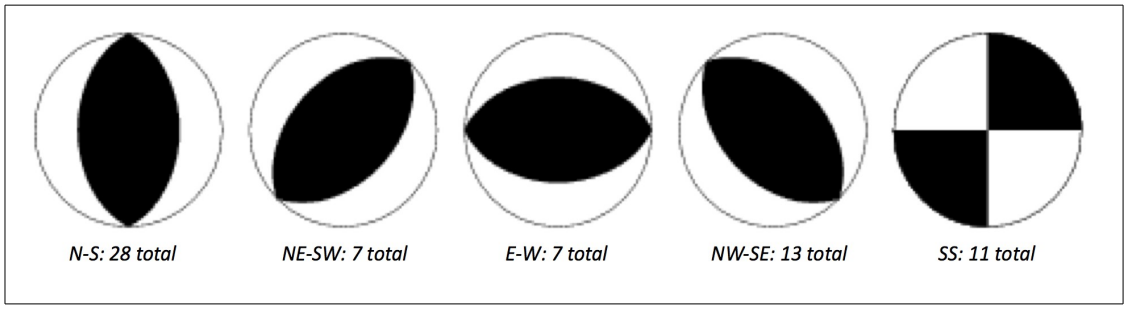

Figure 4.6: The distribution of the 66 well-constrained focal mechanisms. The majority of the mechanisms shows reverse motion, and were therefore broken up into sub-categories by the variation in P-axis trend.

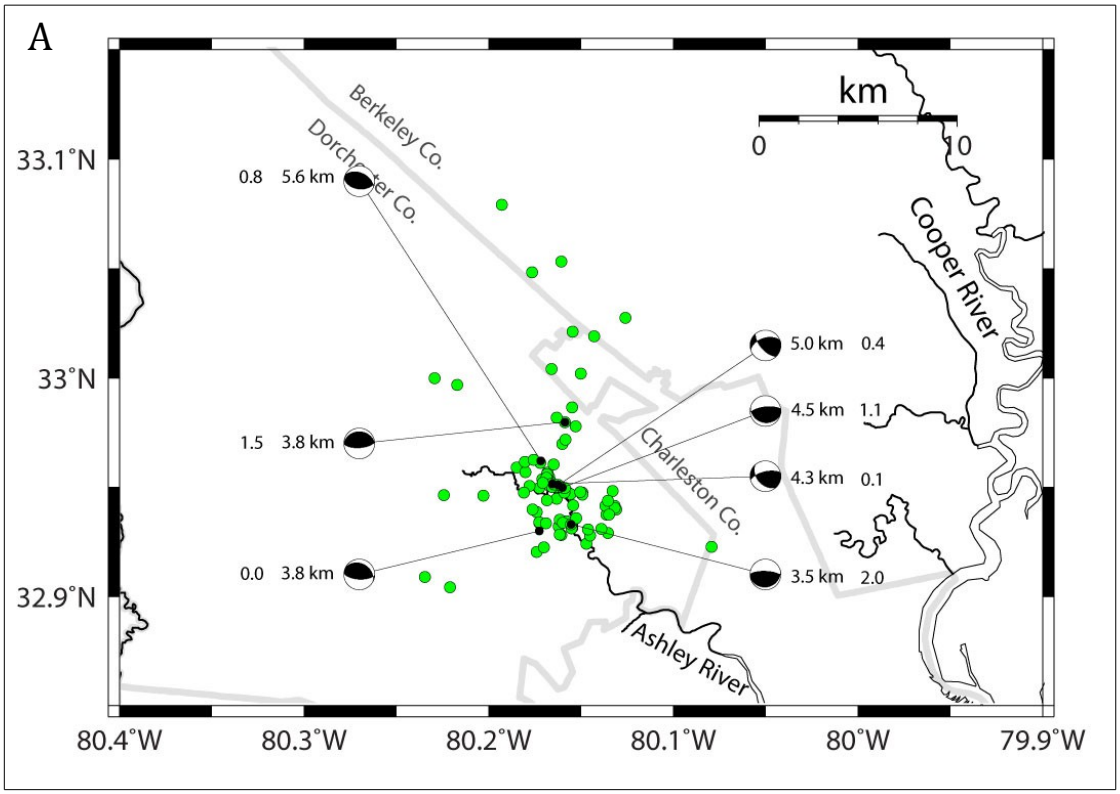
A
km
0
10
Berkeley Co.
Dorchester Co.
Charleston Co.
Cooper River
Ashley River
33.1°N
33°N
32.9°N
80.4°W
80.3°W
80.2°W
80.1°W
80°W
79.9°W
0.8 5.6 km
1.5 3.8 km
0.0 3.8 km
5.0 km 0.4
4.5 km 1.1
4.3 km 0.1
3.5 km 2.0

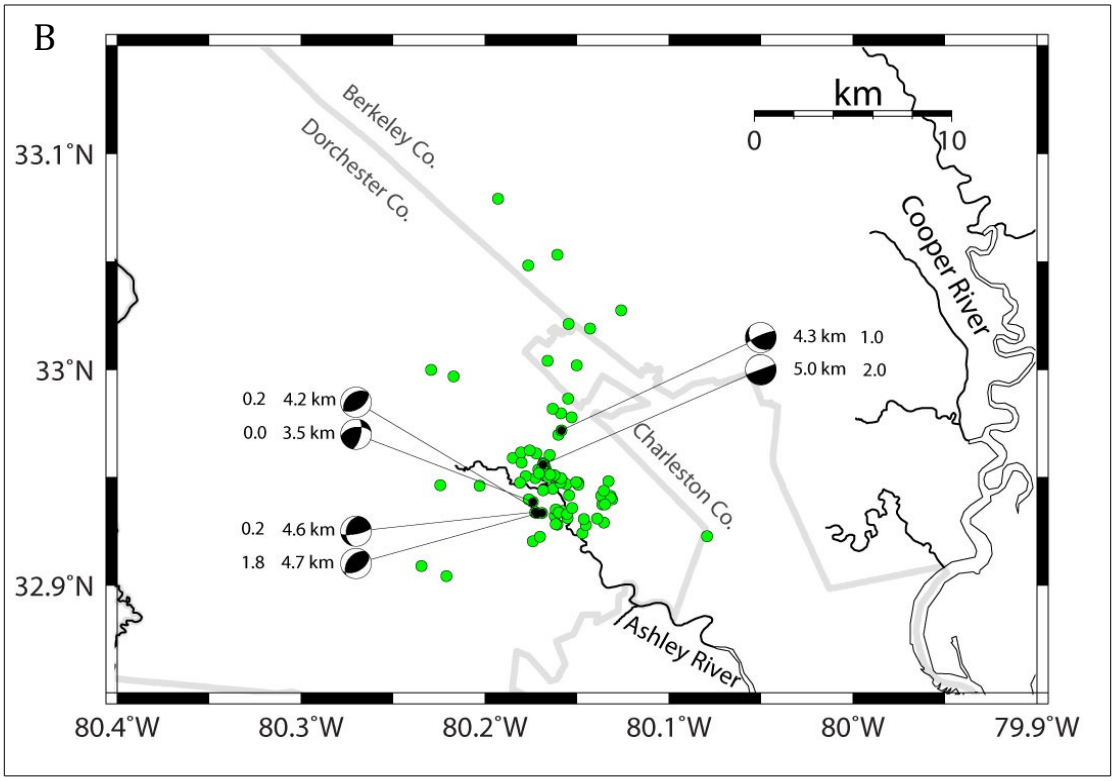
B
km
0
10
Berkeley Co.
Dorchester Co.
Charleston Co.
Cooper River
Ashley River
33.1°N
33°N
32.9°N
80.4°W
80.3°W
80.2°W
80.1°W
80°W
79.9°W
0.2 4.2 km
0.0 3.5 km
0.2 4.6 km
1.8 4.7 km
4.3 km 1.0
5.0 km 2.0

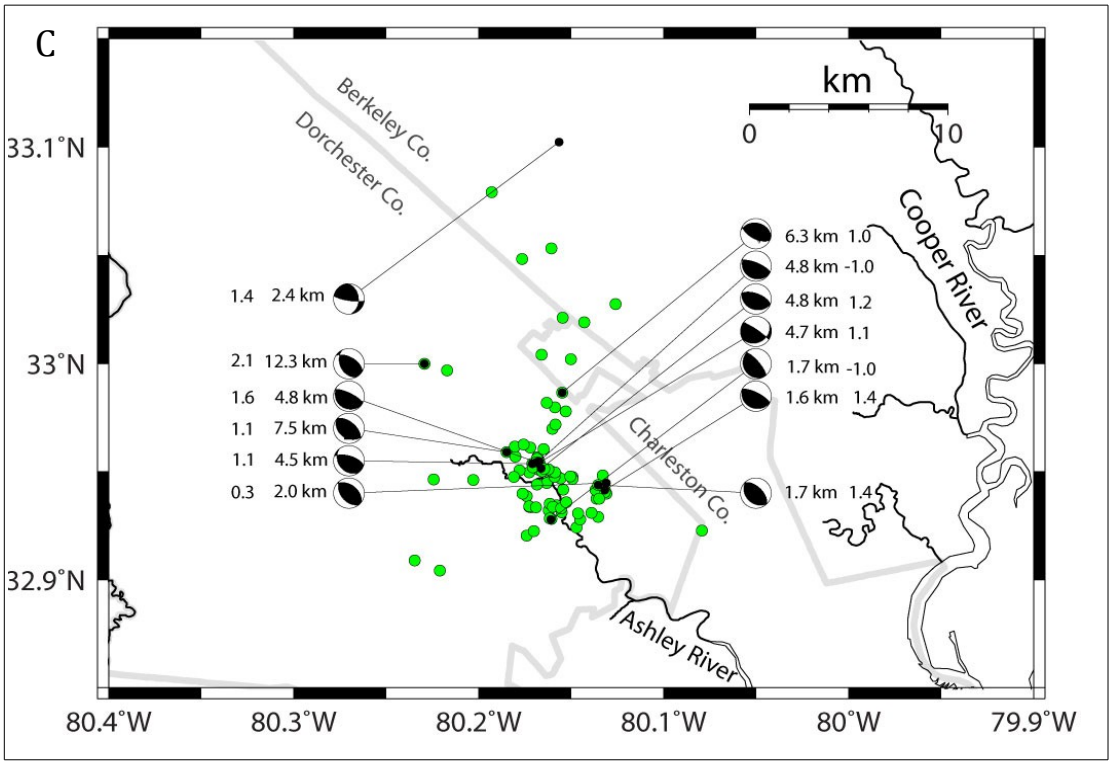
C
km
0
10
Berkeley Co.
Dorchester Co.
Charleston Co.
Cooper River
Ashley River
33.1°N
33°N
32.9°N
80.4°W
80.3°W
80.2°W
80.1°W
80°W
79.9°W
1.4 2.4 km
2.1 12.3 km
1.6 4.8 km
1.1 7.5 km
1.1 4.5 km
0.3 2.0 km
6.3 km 1.0
4.8 km -1.0
4.8 km 1.2
4.7 km 1.1
1.7 km -1.0
1.6 km 1.4
1.7 km 1.4

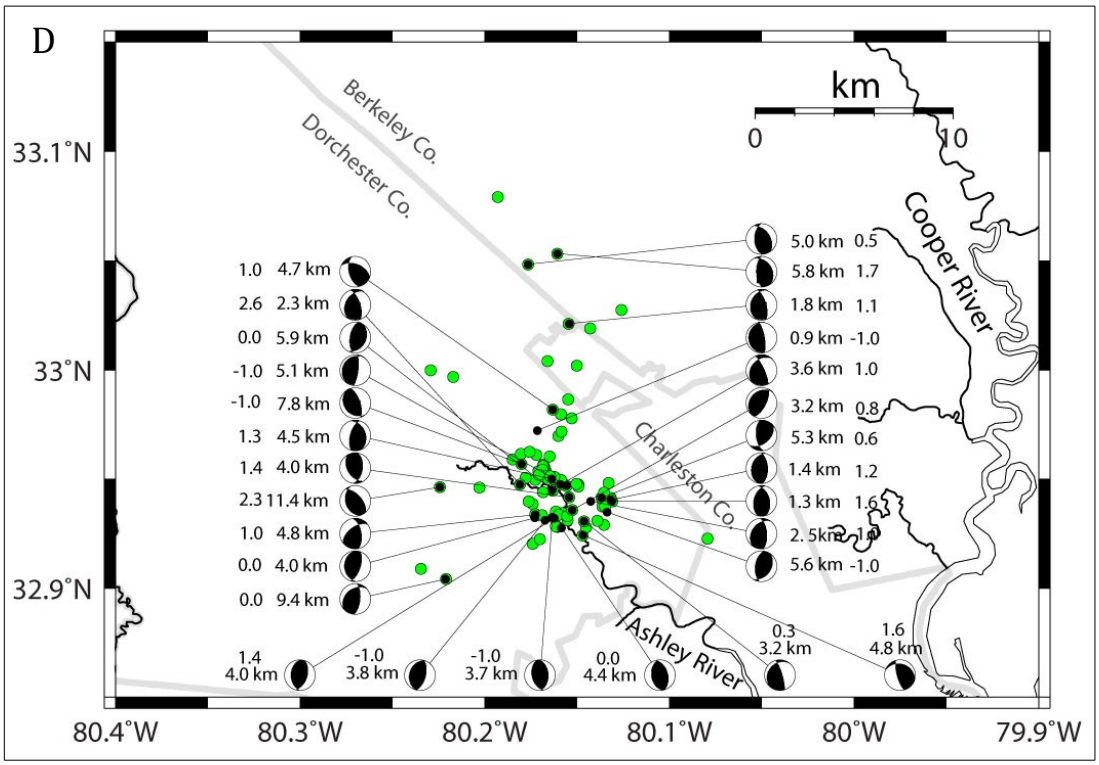
D
km
0
10
Berkeley Co.
Dorchester Co.
Charleston Co.
Cooper River
Ashley River
33.1°N
33°N
32.9°N
80.4°W
80.3°W
80.2°W
80.1°W
80°W
79.9°W
1.0 4.7 km
2.6 2.3 km
0.0 5.9 km
-1.0 5.1 km
-1.0 7.8 km
1.3 4.5 km
1.4 4.0 km
2.3 11.4 km
1.0 4.8 km
0.0 4.0 km
0.0 9.4 km
5.0 km 0.5
5.8 km 1.7
1.8 km 1.1
0.9 km -1.0
3.6 km 1.0
3.2 km 0.8
5.3 km 0.6
1.4 km 1.2
1.3 km 1.6
2.5 km 1.0
5.6 km -1.0
1.4 4.0 km
-1.0 3.8 km
-1.0 3.7 km
0.0 4.4 km
0.3 3.2 km
1.6 4.8 km

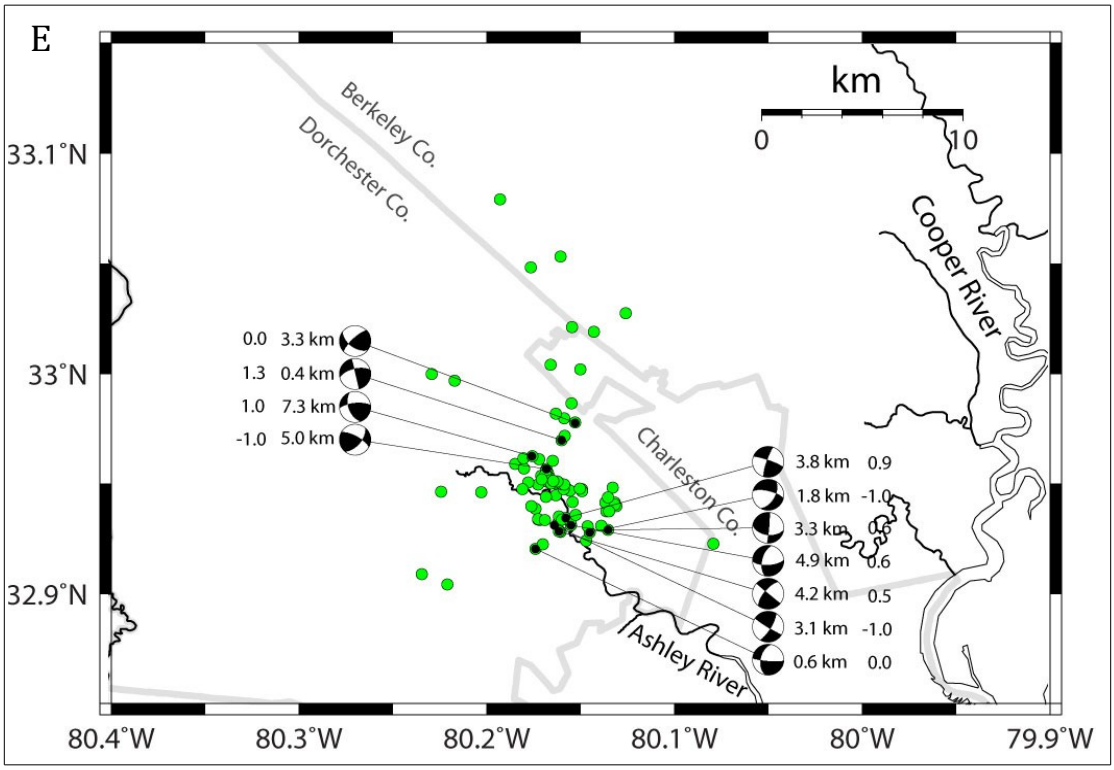

Figure 4.7, A-E: The focal mechanisms plotted with the events relocated using HypoDD. The duration magnitude and focal depth is indicated. The focal mechanisms of each category (defined in Figure 4.6) are shown in panels A through E. A: Reverse motion, E-W trend, 7 total. B: Reverse motion, NE-SW trend, 6 total. C: Reverse motion, NW-SE trend, 13 total. D: Reverse motion, N-S trend, 28 total. E: Strike-slip motion, 11 total.

Appendix B: Tables

Table 1: Network information

Station Name	Latitude (deg., min.)	Longitude (deg., min.)
BBTS	32N58.40	80W06.21
BOSS	33N01.42	80W11.21
CSB	32N59.16	80W04.24
DIVO	32N58.58	80W13.21
MPLC	32N53.66	80W08.77
MTBA	32N55.68	80W09.36
NHSC	33N06.40	80W10.67
PPSC	33N01.59	80W14.33
RGR	32N54.45	80W11.65
TPFD	32N58.79	80W15.22
WSCT	32N56.78	80W07.96

Table 2: Polarity conventions for each phase

Phase	Crest at first half cycle	trough at first half cycle
P	up	down
SH	right	left
SV	forward; away from source	back; towards source

Table 3: Ph2dt parameters

Parameter	Value
Min. Weight	0
Max. Distance (km)	200
Max. Separation (km)	6
Max. Neighbors	20
Min. Link	8
Min. Observations	1
Max. Observations	100

Table 4: HypoDD parameters

Parameter	Value
max. distance (km)	200
Vp/Vs ratio	1.73
IDAT (code for catalog data)	2
IPHA (code for P and S phases)	3
ISOLV (code for LSQR)	2
NLAY (velocity model layers)	4

Table 5: Focmec parameters

Parameter	Value
Vp/Vs ratio at source	1.7321
Max. allowed ratio deviation	0.6*
Maximum no. solutions	500

Table 6: Rating system

Rating	#stations	#polarities
A	≥ 7	≥ 12
B	5-7	8-12
C	4	any
D	3	any

Table 7: Summary of Focal Mechanism Results

Event Name	Type	HE depths	HypoDD depths	# S	# P	# R	rating
20110807_043200_MAN	Rev_NW-SE	7.3	7.536	7	17	12	A
20110816_045000_MAN	SS	2.89	3.29	7	15	11	A
20110818_025100_MAN	Rev_E-W	4.195	5.627	6	14	10	B
20110820_195500_MAN	Rev_N-S	5.6	-	7	17	12	A
20110821_143700_MAN	Rev_NW-SE	2.43	-	8	16	9	A
20110822_061000_MAN	Rev_N-S	3.45	4.04	8	13	8	A
20110822_155900_MAN	SS	3.14	-	4	4	4	C
20110830_071300_MAN	Rev_N-S	4.5	5.88	6	13	2	B
20110913_215900_MAN	Rev_E-W	1.33	-	3	3	2	F
20110922_083300_MAN	SS	3.66	3.826	4	7	8	C
20110929_000900_MAN	Rev_N-S	3.88	4.5	5	9	5	B
20111008_083300_MAN	Rev_N-S	6.9	7.78	5	8	5	B
20111015_070200_MAN	Rev_NW-SE	11.03	12.134	7	16	11	A
20111016_081300_MAN	Rev_N-S	5.62	5.016	4	6	7	C
20111021_221300_MAN	Rev_N-S	4.04	4.811	4	7	6	C
20111027_035100_MAN	Rev_N-S	9.45	9.4	5	8	5	B
20111031_143700_MAN	Rev_E-W	3.57	4.303	5	10	6	B
20111105_164700_MAN	SS	4.56	4.999	5	9	6	B
20111109_090800_MAN	SS	1.96	0.635	4	7	8	C
20111111_232000_MAN	Rev_NW-SE	4.35	4.826	5	15	10	B
20111112_095600_MAN	Rev_N-S	4.62	4.848	8	14	14	A
20111113_022700_MAN	Rev_NE-SW	3.57	3.482	4	9	8	C
20111126_123400_MAN	Rev_NW-SE	4.06	4.51	7	16	11	A
20111206_213800_MAN	Rev_NW-SE	1.83	1.66	4	9	6	C
20111207_094800_MAN	Rev_N-S	1.5	1.341	8	16	8	A
20111211_150300_MAN	Rev_N-S	4.44	5.071	5	6	5	C
20111221_213800_MAN	Rev_N-S	10.88	11.43	9	21	12	A
20111226_101000_MAN	Rev_N-S	3.83	3.57	6	14	10	B
20120102_002000_MAN	Rev_NE-SW	3.6	4.69	8	17	12	A
20120104_075600_MAN	Rev_NE-SW	3.66	4.99	9	19	12	A
20120107_174800_MAN	Rev_NW-SE	4.19	4.67	6	12	6	B
20120109_215700_MAN	Rev_NW-SE	4.15	4.789	9	23	12	A
20120110_063500_MAN	SS	4.62	4.885	5	10	10	B
20120117_061400_MAN	Rev_N-S	2.48	-	4	9	5	C
20120117_114200_MAN	SS	3.08	3.34	4	10	7	C
20120117_125400_MAN	Rev_NW-SE	4.12	-	3	5	4	F
20120119_104800_MAN	Rev_N-S	4.35	-	4	7	3	C
20120120_195300_MAN	Rev_E-W	4.31	4.528	5	10	8	B
20120121_093600_MAN	Rev_NE-SW	4.06	4.583	5	9	7	B

20120128_220400_MAN	Rev_N-S	2.6	1.784	8	15	9	A
20120206_033000_MAN	Rev_E-W	3.76	3.787	10	20	10	A
20120218_113400_MAN	Rev_NW-SE	5.52	6.316	9	18	11	A
20120226_200400_MAN	Rev_N-S	0.86	-	4	6	6	C
20120302_104500_MAN	Rev_N-S	4.23	4.692	5	12	8	B
20120309_195700_MAN	Rev_NE-SW	3.9	4.197	4	8	7	C
20120314_002500_MAN	Rev_N-S	5.26	5.325	5	10	7	B
20120314_062600_MAN	Rev_N-S	3.1	-	3	7	4	F
20120322_120400_MAN	Rev_N-S	6.45	6.584	8	18	14	A
20120325_222800_MAN	Rev_N-S	3.99	-	4	6	3	C
20120326_165200_MAN	Rev_NW-SE	4.35	4.755	5	12	8	B
20120410_040000_MAN	SS	3.95	4.242	4	11	8	C
20120415_013000_MAN	Normal	2.37	-	3	4	4	F
20120509_224700_MAN	Rev_NW-SE	1.69	1.625	6	12	7	B
20120510_212300_MAN	Rev_NW-SE	2.03	-	4	8	6	C
20120511_002100_MAN	Rev_N-S	1.76	1.359	5	9	5	B
20120511_230500_MAN	Rev_NW-SE	1.7	1.73	4	9	6	C
20120516_124100_MAN	Rev_NW-SE	2.06	-	3	5	4	F
20120521_154700_MAN	Rev_E-W	3.05	3.487	8	16	13	A
20120602_092000_MAN	SS	1.66	0.433	7	17	13	A
20120603_064000_MAN	Rev_E-W	4.38	4.958	5	9	7	B
20120625_190500_MAN	SS	2.97	1.76	4	3	3	C
20120709_231000_MAN	Rev_NE-SW	3.88	4.288	5	12	8	B
20120712_204100_MAN	Rev_N-S	2.45	3.184	4	8	6	C
20120720_032100_MAN	SS	7.02	7.283	6	11	10	B
20120728_001600_MAN	Rev_N-S	2.87	3.177	5	12	9	B
20120729_054600_MAN	Rev_E-W	3.76	-	4	6	3	C
20120730_041500_MAN	Rev_N-S	3.81	-	4	6	5	C
20120731_045300_MAN	Rev_N-S	3.56	2.25	10	26	17	A
20120806_083200_MAN	Rev_N-S	3.73	-	4	8	4	C
20120810_172700_MAN	Rev_N-S	3.32	-	3	5	3	F
20120816_033800_MAN	Rev_NE-SW	4.18	4.61	4	9	6	C
20120816_153600_MAN	Near_vert.	4.26	5.585	3	5	6	F
20120829_032500_MAN	Rev_N-S	4.98	5.782	8	15	11	A